Sensitivity of CyGNSS Bistatic Reflectivity and SMAP Microwave Radiometry Brightness Temperature to Geophysical Parameters Over Land Surfaces

Hugo Carreno-Luengo, *Member, IEEE*, Guido Luzi, and Michele Crosetto

***Abstract*—This paper presents an assessment of the correlation between CyGNSS-derived global navigation satellite systems reflectometry (GNSS-R) bistatic reflectivity, Γ_{rl}, and soil moisture active passive (SMAP) derived brightness temperature, $T_I/2$, over land surfaces. This parametric study is performed as a function of soil moisture content (SMC), vegetation opacity τ, and albedo ω. Several target areas, classified according to the International Geosphere-Biosphere Program (IGBP) land cover types, are selected to evaluate potential differentiated geophysical effects on "active" (as many transmitters as navigation satellites are in view) and passive approaches. Although microwave radiometry has potentially a better sensitivity to SMC, the spatial resolution achievable from a spaceborne platform is poor, ∼40 km. On the other hand, GNSS-R bistatic coherent radar pixel-size is limited by half of the first Fresnel zone, which provides about ∼150 m of spatial resolution (depending on the geometry). The main objective of this "active"/passive combination is twofold: a) downscaling the SMC, b) complement the information of microwave radiometry with GNSS-R data to improve the accuracy in SMC determination. The Pearson linear correlation coefficient of Γ_{rl} and $T_I/2$ obtained over Thailand, Argentinian Pampas, and Amazon is ∼−0.87, ∼−0.7, and ∼−0.26, respectively, while the so-called tau–omega model is used to fit the data. Results over croplands are quite promising and deserve special attention since the use of GNSS-R could benefit agricultural and hydrological applications because of: a) the high spatio-temporal sampling properties, b) the high spatial resolution, and c) the potential combination with microwave radiometry to improve the accuracy of the measurements.**

***Index Terms*—CyGNSS, global navigation satellite systems reflectometry (GNSS-R), microwave radiometry, soil moisture active passive (SMAP), soil moisture content (SMC), tau–omega.**

I. Introduction

MICROWAVE remote sensing instruments operating at L-band have shown a good sensitivity to SMC. Higher frequency (i.e., starting from C-band), radiometers, and scatterometers are significantly affected by vegetation cover, while optical sensors additionally suffer from weather conditions and clouds. It is well known that L-band radiometry provides higher sensitivity to SMC as compared with other instruments [1]. Different approaches for SMC determination from space have been implemented, among which: a) ESA's soil moisture ocean salinity (SMOS) mission [1], [2] uses a ∼8 m aperture deployable antenna and a passive synthetic aperture technique to achieve a ∼50 km resolution; b) NASA's soil moisture active passive (SMAP) mission [3], [4] uses a ∼14 rev/min rotating ∼6 m real-aperture reflector antenna, providing ∼40 km of resolution. An adequate performance ∼[0.1, 1] km [5] for applications associated with hydrometeorology, hydrology, and agriculture is however not yet provided.

The use of GNSS L-band signals for Earth remote sensing has been investigated because they were originally proposed for mesoscale ocean altimetry in 1993 [6]. GNSS radio-navigation signals provide global coverage of the Earth's surface and full temporal availability. L-band signals can penetrate clouds, and they are sensitive to SMC, sea ice salinity, snow water content, etc. Global navigation satellite systems reflectometry (GNSS-R) [7]–[9] is a sort of multistatic radar that exploits the numerously available signals of opportunity as provided by the satellite constellations for navigation (GPS, GLONASS, Galileo, Beidou) after being scattered over the Earth's surface. The capability of GNSS-R to perform measurements over points along other directions than Nadir can improve the ability to study the spatio-temporal variability of land-variables, such as SMC and vegetation water content (VWC) [10]–[13]. Direct GNSS signals are mainly right-hand circular polarization (RHCP), with a certain degree of ellipticity. After surface scattering, they become left-hand circular polarization (LHCP); however, the interaction of the electromagnetic waves with the vegetation introduces a copolar term (i.e., RHCP) in the total scattered field [10]–[13]. Additional properties of the GNSS signals should be considered here. There are different correlation techniques to demodulate the signals, so as to extract the geophysical information added to the signals in the scattering process. The interferometric GNSS-R (iGNSS-R) and the conventional GNSS-R (cGNSS-R) are the most widely used [14]. cGNSS-R is appropriate for SMC determination because lower coherent and incoherent integration times are required so that the associated spatial resolution is bet-

Manuscript received February 26, 2018; revised May 23, 2018 and June 28, 2018; accepted July 12, 2018. This work was supported by the Juan de la Cierva Award from the Spanish Ministerio de Economia, Industria y Competitividad, reference FJCI-2016-29356. *(Corresponding author: Hugo Carreno-Luengo.)*

The authors are with the Centre Tecnòlogic de Telecomunicacions de Catalunya/CERCA, Barcelona 08860, Spain (e-mail: hugo.carreno@cttc.cat; guido.luzi@cttc.cat; michele.crosetto@cttc.cat).

Color versions of one or more of the figures in this paper are available online at http://ieeexplore.ieee.org

Digital Object Identifier 10.1109/JSTARS.2018.2856588

ter [15]. The iGNSS-R is devoted to improve the precision (root mean square error RMSE) of altimetric measurements, despite the lower signal-to-noise ratio (SNR).

GNSS-R [9], [16] multistatic radar measurements can potentially be used synergistically with radiometers as a means to improve the spatial resolution in a cost-effective way. GNSS-R uses navigation signals as signals of opportunity so that the platform power requirements are reduced as compared with monostatic radar missions. Furthermore, GNSS-R techniques require relatively small antennas, and thus they can be affordable in constellations of small satellites. At present, there are three missions providing GNSS-R data from space: UK-TDS-1 [17], CyGNSS [18], [19], and SMAP [20], [21]. In this paper, data from CyGNSS 8-microsatellites constellation (LHCP GPS L1 C/A, CYGNSS Level 1 Science Data Record Version 2.0, cGNSS-R) [22]–[24] are used together with SMAP radiometer data (Horizontal-H & Vertical-V polarization, SMAP Level L3 SPL3SMP_E Version 1.0) [25], [26] to evaluate the relationship between the bistatic reflectivity Γ_{rl}, where the subscript rl denotes the incident (r, Right-HCP) and the scattered polarization (l, Left-HCP), and the normalized first Stokes parameter ($T_I/2$), as a function of SMC, vegetation opacity τ, and scattering albedo ω. Section II describes the physics for an appropriate understanding of the fundamentals of microwave radiometry and GNSS-R. Section III provides an overview of the datasets and the methodology. Section IV describes the relationship between Γ_{rl} and $T_I/2$ over selected target areas. Section V discusses the sensitivity of both techniques to SMC, τ, and ω. Finally, Section VI summarizes the main results of this study.

II. Theoretical Elements Toward a Synergistic Use of Microwave Radiometry and GNSS-R Over Land

A. *Interaction of Electromagnetic Radiation With Random Surfaces*

Scattering and emissivity from a random surface are defined through the bistatic scattering coefficient σ^0. This coefficient determines the relationship between the magnitude of the p-polarized incident (incidence and azimuth angles of the i-incident wave are $\theta_{i,i}, \phi_i$; where the subscript i denotes the incident signal) and the q-polarized scattered (incidence and azimuth angles of the s-scattered wave are $\theta_{i,s}, \phi_s$; where the subscript s denotes the scattered signal) electromagnetic fields [27]. The polarized emissivity $e_{g,p}$ in the observation direction is equal to one minus the reflectivity $\Gamma_{g,p}$ [27]

$$e_{g,p}(\theta_{i,i}, \phi_i) = 1 - \Gamma_{g,p}(\theta_{i,i}, \phi_i) \tag{1}$$

where subscript g denotes ground. The reflectivity $\Gamma_{g,p}$ can be calculated as the value of the integral of σ^0 over the upper half space [28]

$$\Gamma_{g,p}(\theta_{i,i}, \phi_i) = \frac{1}{4\pi \cos\theta_{i,i}} \int [\sigma^0_{pp}(\theta_{i,i}, \theta_{i,s}, \phi_i, \phi_s) + \sigma^0_{pq}(\theta_{i,i}, \theta_{i,s}, \phi_i, \phi_s)] d\Omega_s \tag{2}$$

where σ^0_{pp} and σ^0_{pq} are, respectively, the copol and cross-pol components of σ^0, and $d\Omega_s = \sin\theta_{i,s} d\phi_s d\theta_{i,s}$. In the general case, the reflectivity $\Gamma_{g,p}$ is composed of coherent $\Gamma^{\mathrm{coh}}_{g,p}$ and incoherent $\Gamma^{\mathrm{incoh}}_{g,p}$ terms as [29]

$$\Gamma_{g,p}(\theta_{i,i}, \phi_i) = \Gamma^{\mathrm{coh}}_{g,p}(\theta_{i,i}, \phi_i) + \Gamma^{\mathrm{incoh}}_{g,p}(\theta_{i,i}, \phi_i). \tag{3}$$

Then, the emissivity can be modelled using the previous equations as follows:

$$e_{g,p}(\theta_{i,i}, \phi_i) = 1 - \frac{1}{4\pi \cos\theta_i} \left[\int (\sigma^{\mathrm{coh},0}_{pp} + \sigma^{\mathrm{coh},0}_{pq}) d\Omega_s + \int (\sigma^{\mathrm{incoh},0}_{pp} + \sigma^{\mathrm{incoh},0}_{pq}) d\Omega_s \right]. \tag{4}$$

The scattering shape σ^0 for a slightly rough surface follows a delta function along the specular direction ($\theta_{i,i} = \theta_{i,s} = \theta_i$). This dominant term is the coherent one [30], while the incoherent one spreads along all other directions. The formulation of scattering over random surfaces has been deeply studied and several approaches have been proposed. The more widely used models belonging to an analytical solution are the Kirchhoff model (KM) for rough surfaces, and the small perturbation model for slightly rough surfaces. Assuming the coherent scattering term $\sigma^{\mathrm{coh},0}$ is negligible, an expression for the incoherent one can be derived using KM under the geometric optics limit. On the other hand, under the KM with the physics optics approximation, the coherent reflectivity term is modeled as follows [30]:

$$\Gamma^{\mathrm{coh}}_{g,p}(\theta_i, \phi_i) = |R_p(\theta_i)|^2 \exp(-(2k\sigma\cos\theta_i)^2) \tag{5}$$

where R_p is the Fresnel reflection coefficient, k is the signal angular wavenumber, and σ is the surface height standard deviation (SD) (related to surface roughness). The experimental validation of these models was complicated in the past because monostatic radars only measure the backscattering coefficient. The intrinsic bistatic configuration of GNSS-R provides additional information; however, some works have also proposed to measure the backscatter [31]. In the bistatic case, an empirical correction term to determine the effective small-scale roughness was obtained to be as high as ~4 for incident angles $\theta_i \sim 45°$ [32]. Several sounding balloon and space-borne experiments also showed a strong coherent component $\Gamma^{\mathrm{coh}}_{g,p}$ over smooth surfaces such as land [12], [33], and sea-ice [34].

Finally, upon the substitution of (5) in (4), the emissivity $e_{g,p}$ is quantified by

$$e_{g,p}(\theta_i, \phi_i) = 1 - |R_p(\theta_i)|^2 \exp(-2k\sigma\cos\theta_i)^2 - \frac{1}{4\pi\cos(\theta_i)} \int \left[\sigma^{\mathrm{incoh},0}_{pp} + \sigma^{\mathrm{incoh},0}_{pq}\right] d\Omega_s. \tag{6}$$

The emissivity $e_{g,p}$ is estimated by the brightness temperature of the Earth's surface $T_{g,Bp}$ and its effective (physical) temperature T_{Ph} as follows [35]:

$$e_{g,p} = T_{g,Bp}/T_{Ph}. \tag{7}$$

A microwave radiometer provides an estimation of the brightness temperature $T_{g,Bp}$, that over land surfaces depends on the following parameters: θ_i, signal polarization, SMC, vegetation cover, surface temperature, and roughness σ. There are relevant differences between the measured brightness temperatures of smooth and rough surfaces [30]. For smooth surfaces, the incoherent reflectivity $\Gamma_{g,p}^{\text{incoh}}$ is small and thus the emissivity $e_{g,p}$ can be modeled only using the coherent reflectivity term $\Gamma_{g,p}^{\text{coh}}$. Theoretically, the calculation of the coherent reflectivity term $\Gamma_{g,p}^{\text{coh}}$ can be done as the integral value of (2), reducing the integration limits around the specular direction.

B. *Reflectivity Estimation Using GNSS-R Bistatic Radar*

The scattering of GNSS signals is strong over an area around the nominal specular point ($\theta_{i,i} = \theta_{i,s} = \theta_i$). In general, the scattered electromagnetic field contains both a coherent $\sigma^{\text{coh},0}$ and an incoherent contribution $\sigma^{\text{incoh},0}$. The footprint-size associated with the coherent scattering is linked to the size of the first Fresnel zone. On the other hand, the incoherent scattering in a general scenario is limited by the first chip isorange ellipse, with a reduced spatial resolution. Over land surfaces, the scattering of GNSS signals is mainly coherent. Thus, the reflectivity estimation in this bistatic configuration could provide an improved understanding of the models, while complementing the use of microwave radiometers, which provide accurate SMC estimation but a poor spatial resolution.

A GNSS reflectometer measures the power of the Earth's surface-scattered GNSS signals. The main observable is the so-called Delay Doppler Map (DDM) $\langle |Y_r(\tau, f)|^2 \rangle$, where τ is the delay of the signal from the transmitter to the receiver and f is the Doppler shift of the electromagnetic reflected signal. Theoretically, DDMs can be derived under the bistatic radar equation as follows [36], [37]:

$$\left\langle |Y_r(\tau, f)|^2 \right\rangle = \frac{P_T\,\lambda^2}{(4\pi)^3} \iint \frac{G_T\,G_R\,|\chi(\tau, f)|^2 (\sigma^{\text{coh},0} + \sigma^{\text{incoh},0})}{R_T^2\,R_R^2}\, d^2\rho \quad (8)$$

where P_T is the transmitted power, G_T and G_R are the transmitter and receiver antenna gains, respectively, R_T, and R_R are the ranges from the transmitter and the receiver to the specular point, respectively, and χ is the Woodward ambiguity function. The DDMs are therefore composed of two terms

$$\left\langle |Y_r(\tau, f)|^2 \right\rangle = \left\langle |Y_{r,\text{coh}}(\tau, f)|^2 \right\rangle + \left\langle |Y_{r,\text{incoh}}(\tau, f)|^2 \right\rangle. \quad (9)$$

The modeling of the incoherent component $\langle |Y_{r,\text{incoh}}(\tau, f)|^2 \rangle$ has been deeply studied. It was originally derived under the KM with the geometric optics approximation, for a sea surface model with a Gaussian approximation of the slopes [36]. On the other hand, over smooth surfaces such as land, ice, and ocean with low-to-moderate wind-speed conditions, a strong coherent scattering contribution $\langle |Y_{r,\text{coh}}(\tau, f)|^2 \rangle$ to the DDMs has been experimentally measured [12], [33], [34]. At present, several formulations have been proposed to account for these contributions to the DDMs [37]–[40]. They rely on the assumption that the scattering decreases quickly away from the nominal specular reflection point. Under this assumption, the radar equation follows this shape:

$$\left\langle |Y_{r,\text{coh}}(\tau, f)|^2 \right\rangle = \frac{P_T\,\lambda^2\,G_T\,G_R\,|\chi(\tau, f)|^2}{(4\pi)^2\,R^4} \frac{R^2}{4\pi \sin\theta_e} \iint \sigma^{\text{coh},0} d\Omega \quad (10)$$

where $\theta_e = \pi/2 - \theta_i$ is the elevation angle. R is the range from the transmitter to the target over the surface in a monostatic radar configuration. This integral equation can be solved considering the definition of reflectivity in (2), and its application to the coherent scattering case in (5). Then, upon the substitution of (2) and (5) in (10), it is finally derived [37]

$$\left\langle |Y_{r,\text{coh}}(\tau, f)|^2 \right\rangle = \frac{P_T\,\lambda^2\,G_T\,G_R\,|\chi(\tau, f)|^2}{(4\pi)^2\,R^2} |R_p(\theta_i)|^2 \exp\left(-2k\sigma\cos\theta_i\right)^2. \quad (11)$$

If the image method for a specular reflection is applied to the Friis transmission formula, the transmitter sees its image in the reflection [28]. In this situation, the geometry can be modeled as two antennas separated a distance $R = R_T + R_R$. An effort to provide a GNSS-R unified-model based on the bistatic radar equation, without the assumption of image theory, showed that in the case of the coherent scattering, the reflected power is roughly independent of R_R ($R_T \gg R_R$) as follows:

$$\left\langle |Y_{r,\text{coh}}(\tau, f)|^2 \right\rangle = \frac{P_T\,\lambda^2\,G_T\,G_R\,|\chi(\tau, f)|^2}{(4\pi)^2\,(R_T + R_R)^2} |R_p(\theta_i)|^2 \exp\left(-2k\sigma\cos\theta_i\right)^2. \quad (12)$$

In the derivation of this equation, it was found that the equivalent area from which the coherent scattered signal comes from is $1/\sqrt{\pi}$ times the projection over the surface of the first Fresnel zone [41].

The reflectivity $\Gamma_{g,rl}$ is estimated as the ratio of the reflected $Y_{r,\text{Peak}}$ and the direct $Y_{d,\text{Peak}}$ power waveforms peaks [42], after compensation of the noise power floor and the antenna gains, as a function of the elevation angle

$$\Gamma_{g,rl} = \left\langle |Y_{r,\text{Peak}}|^2 \right\rangle \Big/ \left\langle |Y_{d,\text{Peak}}|^2 \right\rangle. \quad (13)$$

C. *Effects of Vegetation on Microwave Signals*

Equations (5) and (6) provide the link between $e_{g,p}$ and $\Gamma_{g,p}$ for a random rough surface. Earth's surface is mostly covered by different levels of vegetation that modifies this link. The understanding of vegetation effects on the geophysical relationship between $e_{g,p}$ and $\Gamma_{g,p}$ is relevant for: a) SMC determination, and b) to develop downscaling techniques using GNSS-R. The radiative transfer (RT) theory is a heuristic approach to model the transport of intensity through a random medium [43]. The so-called tau–omega ($\tau - \omega$) model is the zeroth order solution to the nonscattering RT equations and it provides an approximation of the vegetation effects for low frequencies, such as

This article has been accepted for inclusion in a future issue of this journal. Content is final as presented, with the exception of pagination.

L-band. The optical depth τ and the single-scattering albedo ω parameterise the properties of the vegetation attenuation and the scattering effects (structural changes), respectively. The general expression is as follows [44], [45]:

$$T_{Bp} = T_S(1-\Gamma_{g,p})\gamma + T_v(1-\omega)(1-\gamma) + T_v(1-\omega)(1-\gamma)\Gamma_{g,p}\gamma \tag{14}$$

where T_S and T_v are the effective temperatures of the soil and the vegetation, respectively, and γ is the transmissivity of the vegetation layer. Most studies consider as a valid approximation that $T_S \approx T_v$ [45]. The first term is the radiation from the soil attenuated by the vegetation. The second term is the radiation directly from the vegetation, while the third term defines the downward radiation from the vegetation, reflected upward by the soil and again attenuated by the canopy. The transmissivity of the vegetation γ can be defined in terms of τ and θ_i

$$\gamma = e^{-\tau/\cos\theta_i}. \tag{15}$$

τ depends on the signal polarization and θ_i [46], especially for vegetation canopies with dominant vertical structures. τ can be linearly related with the VWC for low vegetated areas, while there is a good correlation with the normalized difference vegetation index (NDVI) and leaf area index for a wider range of vegetation types including forest [45]. At L-band, it is worth noting that: a) leaves are almost transparent, and attenuation is mainly due to branches [44]; b) the dependence of ω with θ_i should be considered for the GNSS-R case [12], [33].

III. Data and Methods

A. CyGNSS and SMAP Data

CyGNSS's highest-priority mission objective is the study of tropical cyclones. Thus, the selected orbital configuration of each of these 8-GNSS-R receivers (operating at a frequency of 1.575 GHz) is a circular low Earth orbit with an inclination angle of 35°. Each single satellite has two ∼14.5 dB-gain LHCP antennas pointing to the Earth's surface with an inclination angle of 28° (antenna boresight). In this paper, the application of CyGNSS is extended to land surfaces studies. In this scenario, the scattering is mostly coherent, so that the spatial resolution is limited by approximately half of the first Fresnel zone, i.e., ∼150 m (depending on the geometry) [41].

SMAP's highest-priority mission objective is to provide global (and thus, the operation from a Sun-synchronous orbit (SSO), with 6 A.M.–6 P.M. equatorial crossing times) SMC maps with a resolution of at least ∼10 km and with an accuracy of $0.04\,\mathrm{cm}^3/\mathrm{cm}^3$ unbiased RMSE [26]. This is achieved using the combination of active–passive information. SMAP's 36 dB-gain dual-polarization (H & V) antenna reflector points to the Earth's surface with an incident angle of $\theta_i \sim 40°$. The approximately constant incident angle simplifies the data processing and enables accurate repeat pass for SMC estimation. Unfortunately, the radar high-power amplifier failed on 7th July 2015, leaving only the possibility to operate the receiver as a radiometer. In this paper, radiometer (operating at a frequency of 1.227 GHz) data are used. SMAP measures the brightness temperature T_{Bp} at the two linear polarizations (H & V). The polarization of an electromagnetic wave can be represented by the four Stokes parameters I, Q, V,U. The first Stokes I describes the total intensity of electromagnetic emission, and it is of interest in this paper. In polarimetric passive remote sensing, the Stokes parameters are usually expressed in terms of brightness temperature. The normalized first Stokes parameter T_I is defined as follows [47]:

$$T_I/2 = (T_{B_H} + T_{B_V})/2 = \frac{\lambda^2}{k_B B_w} I/2 \tag{16}$$

where k_B is the Boltzmann constant, and B_w is the noise bandwidth. $T_I/2$ provides a valuable measurement of the total brightness temperature at circular polarization [48].

In this paper, an evaluation on the geophysical relationship between CyGNSS-derived reflectivity [22]–[24] and SMAP-emissivity [25], [26] is performed using the corresponding online available missions' products.

CYGNSS Level 1 Science Data Record is used to estimate the bistatic reflectivity using the direct and reflected calibrated DDMs [49], based on the on-flight DDMs generated by the delay Doppler mapping instrument (DDMI) [50], [51]. The calibrated reflected and direct DDMs are used to estimate the power waveforms peaks $Y_{r,\mathrm{Peak}}$ and $Y_{d,\mathrm{Peak}}$; computed using 1-ms coherent integration time, followed by 1000 incoherent averages. The estimation of the CyGNSS reflectivity is obtained applying (13) after compensation of the antennas' gain patterns versus the gain at the corresponding boresight direction [down-looking gain ~ 14.5 dB, $\theta_i = 28°$ and up-looking gain ~ 4.7 dB, $\theta_i = 0°$], and the difference of both gains at boresight. The compensation of the antennas' gain is performed as a function of θ_i, with a precision of four decimals. This is important for a correct estimation of Γ_{rl} because the transmitted signal power depends on θ_i, and because both gain patterns have a different dependence with this variable. The following CYGNSS Level 1 Science Data Record variables are used in this procedure: DDM signal to noise ratio and Zenith signal to noise ratio for the estimation of $Y_{r,\mathrm{Peak}}$ and $Y_{d,\mathrm{Peak}}$; while Specular point Rx antenna gain for the information of the down-looking antenna gain in the direction of the specular point. The up-looking antenna is an omnidirectional one with a ∼4.7 dB gain at the antenna boresight and a half-power beam-width of ∼57° [24]. The application of a moving averaging filter minimizes potential residual errors in the down-looking antenna gain pattern correction due to attitude determination and control system (ADCS) and in the estimation of the reflected and direct power peaks. The main goal of this filter is to provide monthly averaged values of Γ_{rl}, $T_I/2$, SMC, τ, and ω. The geometrical power losses [52] are autocalibrated using (13) because the coherent scattering (12) is roughly independent of R_R ($R_T \gg R_R$). Additionally, as a quality control, reflected DDMs used for the reflectivity estimation were selected with SNR values higher than 3 dB.

On the other hand, the SMAP Enhanced L3 Radiometer Global Daily 9-km Level L3 SPL3SMP_E Version 1.0 product is used. It is derived from the SMAP‘s radiometer (6 A.M.–6 P.M. data in separate arrays) and ancillary data, over the global 9-km

This article has been accepted for inclusion in a future issue of this journal. Content is final as presented, with the exception of pagination.

Equal-Area Scalable Earth (EASE 2.0) grid [26], [53]. The main variables used along this paper are described here:

1) Brightness temperature (T_{Bp}): It is the arithmetic average of L1B_TB's p polarized brightness temperature interpolated at 9-km using the Backus–Gilbert technique. This approach allows the use of additional radiometric information that was not available for the baseline product because the original brightness temperature product was oversampled in the along-track direction [53]. Water brightness temperature correction is applied to this parameter before SMC inversion.
2) Soil moisture content (SMC): The SMC retrieval is based on the application of the single channel algorithm at V-pol [26], [54], when favorable surface conditions are identified at a given grid cell. Then, corrections for surface roughness, effective soil temperature, and VWC are applied.
3) Vegetation opacity τ: The retrieval is based on a priori NDVI information obtained from visible-near infrared reflectance data from the NPP/JPSS VIIRS instrument, and land cover type assumptions [26], [54]. It is used to retrieve γ as an estimation of the attenuation of the electromagnetic signal through the vegetation layer.
4) Single-scattering albedo ω: These data are classified by type of land cover and delivered to the SCA-V by means of a LUT [26], [54]. This parameter serves as an estimation of the fractional signal power scattered by the vegetation.

B. Gridding and Target Areas

The selected temporal data-window corresponds to September–October 2017 (one month). High SMC values, and no ice/snow over the monitored surfaces are expected during the first weeks of autumn (North hemisphere), and spring (South hemisphere). The selected temporal length of this filter is one month because if the temporal window is too small (e.g., one week) there are few points in the regression and probably also a lack of temporal fluctuations of geophysical parameters in most of the target areas over the Earth. The study of the geophysical relationship between Γ_{rl} and $T_I/2$ is improved as larger is their variability, and thus one month is a reasonable temporal length. On the other hand, the seasonal changes could not be captured if the temporal length is too long (e.g., several months or one year) because the variability will be averaged. GNSS-R sampling characteristics are nonhomogeneous since they depend on the geometry [55]. On the other hand, SMAP's antenna boresight rotates $\sim$14 rev/min about Nadir, providing a $\sim$1000 km wide-swath. CyGNSS data associated with incidence angles $\theta_i = [30°, 50°]$ around the SMAP's antenna boresight were considered here to minimize the effect of θ_i on Γ_{rl}, while optimizing the number of samples available for this study.

A 0.1° by 0.1° latitude/longitude grid was selected and data were averaged using a moving window of 0.2° at steps of 0.1° (see Fig. 1). The associated spatial resolution is $\sim$20 km at equatorial latitudes. This strategy was found to provide a better performance as compared with smaller windows (see Tables I and II). The larger window's size provides an improved filtering of potential short-term fluctuations of brightness temperature and reflectivity (footprint $\sim$500 m across-track/$\sim$7.6 km along-track; orbital height $\sim$500 km, $\theta_e \sim 60°$) due to different noise sources, such as ADCS and geolocation of the nominal specular point. Additionally, a larger window-size reduces the impact of neither spatially nor temporally collocated CyGNSS and SMAP measurements. On the other hand, a smaller window is less sensitive to the effects of land cover heterogeneity, and thus, the SD of the measurements is lower (see Table II and Fig. 2). However, the correlation between both sensors increases for a larger window because, in addition to previous reasons, this size smooths the effect of the different spatial resolutions of both sensors. A 0.04° window provides a spatial resolution approximately similar to that of the coherent scattering term $\sim 4\,\text{km}^2$. On the other hand, the spatial resolution of the SMAP enhanced radiometer product is $\sim 81\,\text{km}^2$. Aggregating reflectivity data over larger areas provides a product associated with the similar geophysical parameters that the radiometer is detecting at each measurement.

Different target areas can be monitored belonging to a wide variability of land-surface types based on their dominant IGBP land cover types (see Table I) obtained from the moderate resolution imaging spectrometer (MODIS) Terra+Aqua combined MCD12Q1 product [56]: Sahara (Barren), Pampas (Cropland), Thailand (Cropland), US Midwest (Grassland), Murrumbidgee (Open Shrubland), Tanzania (Savanna), Northeast Region of Brazil (Woody Savanna), and Amazon (Evergreen Broadleaf Forest). MODIS IGBP data at 500-m spatial resolution is an open access product [56]. In this paper, IGBP data is displayed using a 0.1° by 0.1° latitude/longitude grid [see Fig. 1(a)]. Table II summarizes this information while providing complementary information about the RVI [57]–[59], and the GSI [60].

RVI is an index of vegetation structure. It is independent of vegetation greenness, and it can be used to characterize the vegetation scattering due to structural elements. It can be estimated [59], [61] as follows:

$$\mathrm{RVI} = \frac{8\sigma_{\mathrm{HV}}}{\sigma_{\mathrm{HH}} + \sigma_{\mathrm{VV}} + 2\sigma_{\mathrm{HV}}} \tag{17}$$

where σ_{pq} are the radar backscatter cross sections; in this paper, they correspond to the aquarius/SAC-D mission polarimetric radar product [59], [61]–[63]. RVI ranges from zero for bare soil, to the unity for dense vegetation.

GSI was first introduced in [60] to measure the degree of concentration when individuals are classified into types; as such it is generally used in ecology. Here, GSI is used as an indicator of the land cover heterogeneity. It can be calculated as in [61]

$$\mathrm{GSI} = 1 - \sum p_i^2 \tag{18}$$

where p_i is the relative portion of pixels that determines the IGBP class i from MODIS. It ranges from zero to the unity when the heterogeneity is large.

IV. Spaceborne Bistatic Reflectivity and First Stokes Parameter Data Functional Relationship

SMAP's L-band radiometer measures the microwave emission in the form of the brightness temperature $T_I/2$, while

This article has been accepted for inclusion in a future issue of this journal. Content is final as presented, with the exception of pagination.

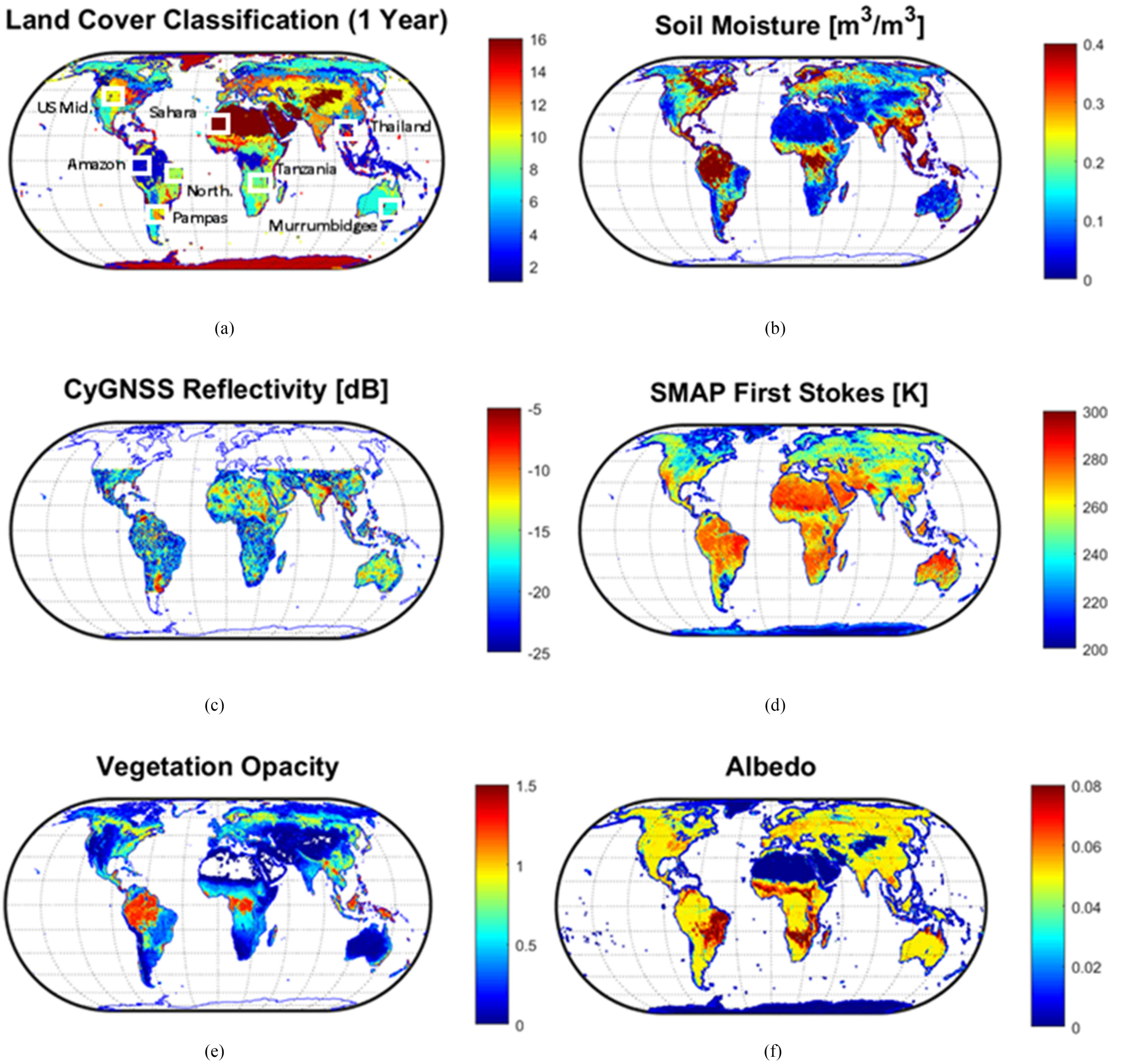

Fig. 1. (a) International geosphere-biosphere program (IGBP) land cover classification (see Table I). (b)–(f) 1-month (20/09/2017–20/10/2017) mean values over land surfaces: (b) SMC values derived from the SMAP's radiometer enhanced product [53], (c) CyGNSS reflectivity Γ_{rl}, (d) normalized SMAP radiometer first Stokes parameter $T_I/2$, (e) vegetation opacity τ, and (f) single-scattering albedo ω. Window-size of $0.2° \times 0.2°$.

CyGNSS's L-band GNSS reflectometer measures the fraction of energy forward-scattered Γ_{rl} after transmission of the navigation signals of opportunity. The scattering of GNSS signals is mainly coherent $\langle |Y_{r,\mathrm{coh}}(\tau, f)|^2 \rangle$, as an indication of the dominant contribution of the soil [33], [39], [64]. Here, spaceborne data were analyzed to improve our understanding of the geophysical relationship between Γ_{rl} and $T_I/2$. The relationship was studied over the selected target areas as a function of SMC, τ, and ω. The goal of the synergistic use of both type of sensors is to improve the SMC determination and to that end, the effect of vegetation (τ and ω) should be considered. Fig. 1(a) shows the IGBP land cover classification. Fig. 1(b)–(f) shows 1-month of averaged values of SMC [see Fig. 1(b)], Γ_{rl} [see Fig. 1(c)], $T_I/2$ [see Fig. 1(d)], τ [see Fig. 1(e)], and ω [see Fig. 1(f)], using a window of $0.2° \times 0.2°$.

CyGNSS mission provides coverage of the Earth's surface in the latitude range $\sim [-40°, 40°]$, and thus, only a limited number of land cover types can be studied [see Fig. 1(a) and (c)]. SMAP mission provides global coverage of the Earth because it operates from an SSO orbit. Over latitudes $\sim [-40°, 40°]$, the Earth's surface is covered by numerous deserts and tropical rainforests. As such, this paper allows the study over regions with highly differentiated values of SMC [see Fig. 1(b)], τ [see Fig. 1(e)] and ω [see Fig. 1(f)]. τ values, associated to signal

TABLE I
IGBP LAND COVER CLASSIFICATION

1	Evergreen needleleaf forest	**9**	Savannas
2	Evergreen broadleaf forest	**10**	Grassland
3	Deciduous needleleaf forest	**11**	Permanent wetlands
4	Deciduous broadleaf forest	**12**	Croplands
5	Mixed forest	**13**	Urban and built-up
6	Closed shrublands	**14**	Cropland/Natural veg. mosaic
7	Open shrublands	**15**	Snow and ice
8	Woody savannas	**16**	Barren or sparsely vegetated

TABLE II
LATITUDE AND LONGITUDE OF THE SELECTED TARGET AREAS

	Thailand	**Pampas**	**Tanzania**	**Amazon**	**US**	**Murrumbidgee**	**Northeast**	**Sahara**
Lat [º]	[15,20]	-[37,30]	-[9,2]	[-8,1]	[32,39]	-[35,31]	-[15,4]	[19,26]
Lon [º]	[98,105]	-[65,60]	[29,35]	-[75,65]	-[105,85]	[141,148]	-[46,39]	[-15,3]
Pearson. High window	-0.87	-0.7	-0.49	-0.26	-0.25	-0.12	-0.09	-0.06
Pearson. Medium window	-0.77	-0.63	-0.46	-0.26	-0.23	-0.09	-0.06	-0.04
Pearson. Low window	-0.71	-0.52	-0.4	-0.2	-0.14	-0.08	-0.01	-0.02
SD Γ_{rl} [dB] High window	3.4	2.2	2.6	3.2	2.8	2.8	1.8	1.9
SD Γ_{rl} [dB] Medium window	2.4	1.8	1.9	2.3	2	2	1.1	1.5
SD Γ_{rl} [dB] Low window	0.7	0.7	0.6	0.5	0.6	0.7	0.3	0.5
SD $T_I/2$ [K] High window	2.8	6.7	6.6	1.3	7.3	6.8	2.1	5
SD $T_I/2$ [K] Medium window	1.7	5.6	3.1	0.8	4.9	3.5	1.2	2.3
SD $T_I/2$ [K] Low window	0.5	5.1	1.4	0.3	4.5	2.8	0.6	1.9
IGBP	Cropland	Cropland	Savanna	Evergreen Broadleaf Forest	Grassland	Open Shrublands	Woody Savanna	Barren
RVI	0.81	0.39	0.8	1	0.65	0.69	0.87	0.12
GSI	0.52	0.48	0.72	0.04	0.79	0.43	0.35	0
α [K] High window	270.8	249.5	268.3	286.2	264.2	277.5	289.9	260.3

For each of these areas: Pearson lineal correlation coefficient r between CyGNSS reflectivity Γ_{rl} and SMAP radiometer normalized brightness temperature $T_I/2$, SD of the pixels-SD corresponding to Γ_{rl} and $T_I/2$, radar vegetation index (RVI), Gini–Simpson index (GSI), and best fit parameter α of the tau–omega model for the geophysical relationship between Γ_{rl} and $T_I/2$. The Pearson coefficients and the SD are provided for three different window-size: High (0.1° × 0.1°;0.2°), medium (0.1° × 0.1°;0.1°), and small (0.02° × 0.02°;0.04°). α parameters are provided for the high window-size.

attenuation due to canopy layer, appear higher over tropical rainforests because this parameter is related to the wet biomass [65]. ω values, associated with incoherent scattering effects, are higher over drylands with forests such as woody savannas (dry biomass) [66], because it is related with land-cover type heterogeneity and structural effects of the canopy layer [65].

Figs. 3–5 show the scatter plots of $T_I/2$ against Γ_{rl} measurements over Amazon [see Fig. 3(a), (d), and (g)], Thailand [see Fig. 3(b), (e), and (h)], Argentinian Pampas [see Fig. 3(c), (f), and (i)], Tanzania [see Fig. 4(a), (d), and (g)], US Midwest [see Fig. 4(b), (e), and (h)], Murrumbidgee [see Fig. 4(c), (f), and (i)], Sahara [see Fig. 5(a), (c), and (e)], and the Northeast Region of Brazil [see Fig. 5(b), (d), and (f)]. The range of Γ_{rl} is the same for all the plots, and the ranges of $T_I/2$, SMC, τ, and ω were adapted to each target area. This strategy was assumed to provide intercomparable plots, and at the same time showing full variability. The order in the figures was established as a function of decreasing SMC levels, from tropical rainforests to arid deserts. The Pearson correlation coefficients r (see Table II) follow this decreasing order: $r_{\text{Thailand}} \sim$ –0.87, $r_{\text{Pampas}} \sim$ –0.7, $r_{\text{Tanzania}} \sim$ –0.49, $r_{\text{Amazon}} \sim -0.26$, $r_{\text{US}} \sim -0.25$, $r_{\text{Murrumbidgee}} \sim -0.12$, $r_{\text{Northeast}} \sim -0.09$, and $r_{Sahara} \sim -0.06$. A wide range of SMC can be observed over all the target areas from dry soils to wet soils, except over Sahara and Northeast regions. This provides a useful framework to evaluate the correlation between both sensors. An inverse relationship was found between CyGNSS and SMAP passive observations with SMC, which in

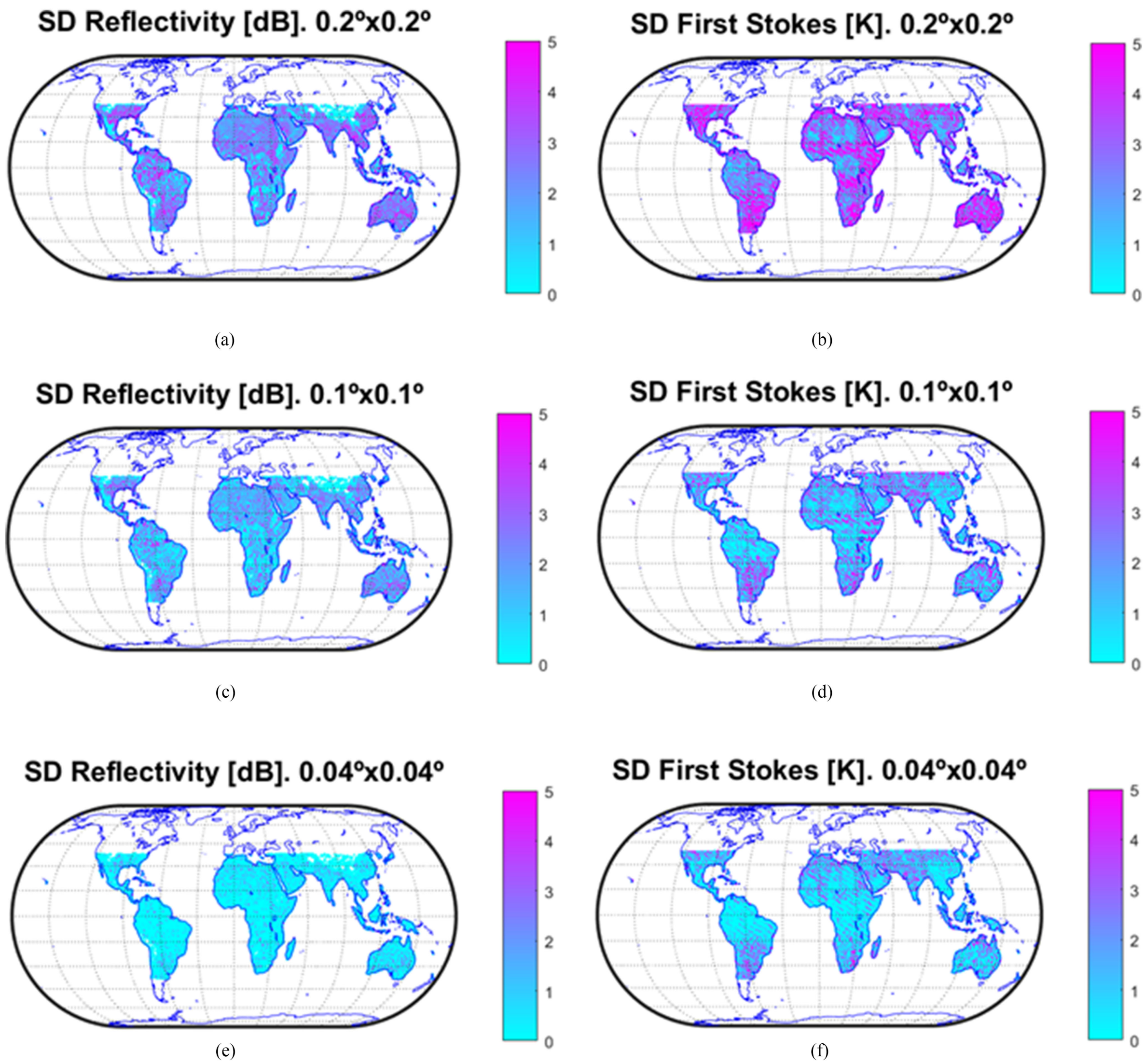

Fig. 2. Effect of the moving averaging window-size (a), (b) $0.2° \times 0.2°$, (c), (d) $0.1° \times 0.1°$, and (e), (f) $0.04° \times 0.04°$, in the SD of CyGNSS Reflectivity Γ_{rl} (a), (c), (e) and SMAP first Stokes parameter $T_I/2$ (b), (d), (f).

turns reflects the expected sensitivity to changes in the dielectric constant of the soil [67]. This functional relationship between both types of sensors is different from that associated with previous SAR-based studies [61], [68]. The tau–omega model (14) under the assumption $T_S \approx T_v \approx \alpha$, where α is the coefficient of regression, was used to fit the scatter plots of Γ_{rl} versus $T_I/2$ (see Figs. 3–5). The coefficients α were obtained using an iterative least square estimator. The results are summarized in Table II. This fit, based on the tau–omega model, shows sensitivity to the α parameter in addition to r. This is important in the potential development of microwave radiometry downscaling techniques based on time series statistical analysis of radiometer–reflectometer data functional relationship such as in [69].

A. Amazon, Thailand, and Pampas: High SMC Levels

Fig. 3 shows the analysis over Amazon [see Fig. 6(a)], Thailand [see Fig. 6(b)], and Argentinian Pampas [see Fig. 6(c)], with high SMC, high-to-moderate RVIs [$\mathrm{RVI}_{\mathrm{Amazon}} \sim 1, \mathrm{RVI}_{\mathrm{Thailand}} \sim 0.81$, and $\mathrm{RVI}_{\mathrm{Pampas}} \sim 0.39$], and low-to-moderate GSIs [$\mathrm{GSI}_{\mathrm{Amazon}} \sim 0.04, \mathrm{GSI}_{\mathrm{Thailand}} \sim 0.52$, and $\mathrm{GSI}_{\mathrm{Pampas}} \sim 0.48$]. The dominant IGBP land cover type over the Amazon target area is evergreen broadleaf forests (IGBP 2). The mean canopy height is ~40 m, and the region is covered with a significant amount of rivers [70]. The dominant IGBP over Thailand (IGBP 14) and the Argentinian Pampas (IGBP 12) is croplands. Croplands are normally vegetated areas with different levels of VWC, and with homogeneous surface roughness levels due to agricultural activities. Two different types of croplands with differentiated VWC levels are selected for this study. Thailand is characterized by irrigated rice production and tropical forests. On the other hand, Pampas is a quite flat homogeneous terrain.

The $T_I/2$ dynamic ranges decrease from ~120 K (Thailand) and ~100 K (Pampas) to ~30 K (Amazon). The radiometer measurements over densely vegetated areas (e.g., Amazon) and deserts have a low SNR, which could introduce some degree of uncertainty in the interpretation of the results. On the other hand, the Γ_{rl} ranges seem to be less affected by the vegetation

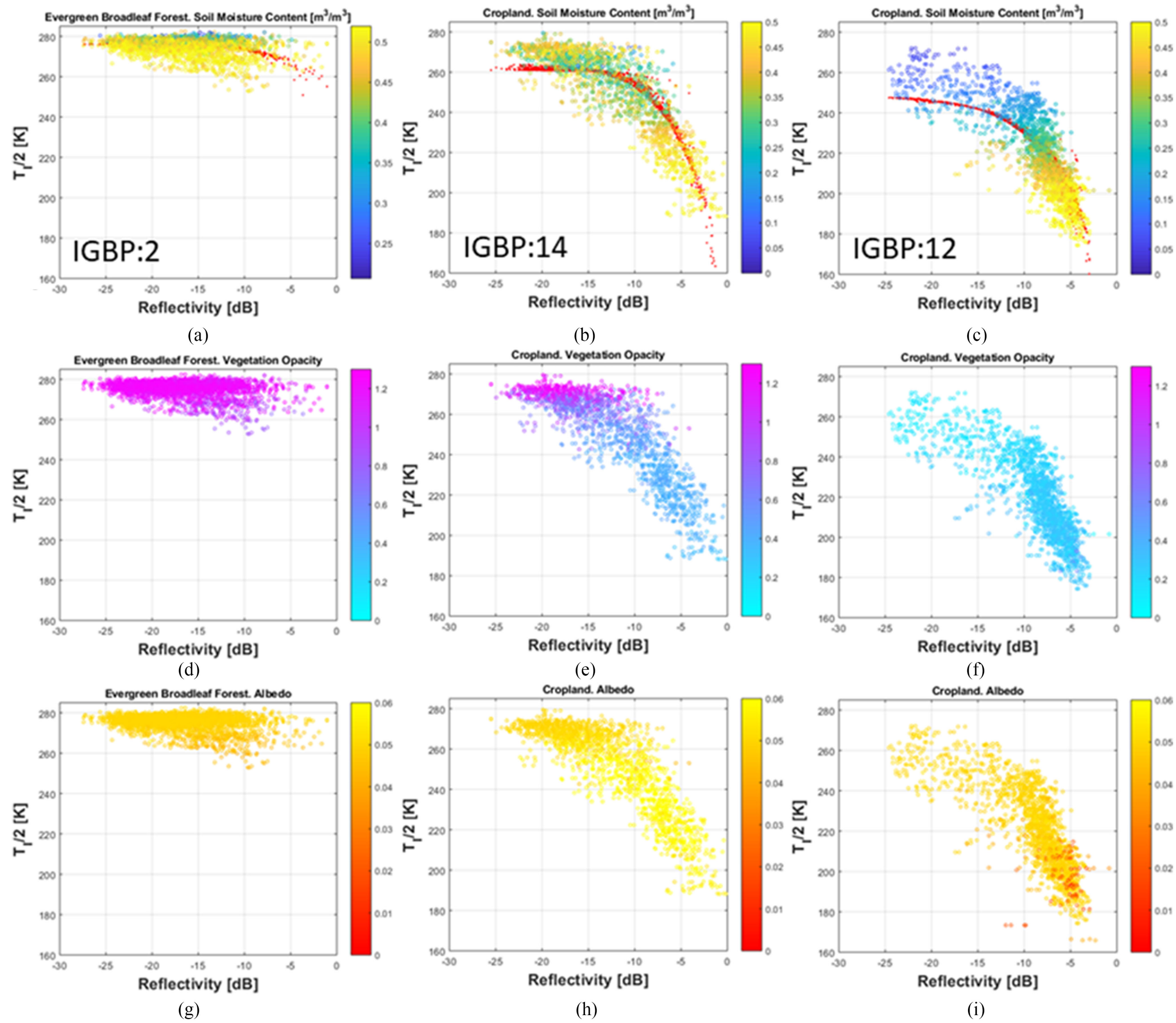

Fig. 3. Relationship between CyGNSS reflectivity Γ_{rl} and SMAP radiometer normalized brightness temperature $T_I/2$, as a function of (a)–(c) SMC, (d)–(f) vegetation opacity τ, and (g)–(i) albedo ω; and for different target areas (a), (d), (g) Amazon, (b), (e), (h) Thailand, and (c), (f), (i) Pampas. In (a)–(c), tau–omega model used to fit the scatter-plots is also depicted (red dots).

cover: $\sim$25 dB (Thailand) [see Fig. 6(b)], $\sim$20 dB (Pampas) [see Fig. 6(c)] and $\sim$28 dB (Amazon) [see Fig. 6(a)]. This seems to indicate that GNSS-R signals can partially penetrate through the vegetation [20], being the scattering dominated by the soil. An interpretation of the results is provided for each target area.

Over the Amazon [see Fig. 3(a), (d), and (g)], the $T_I/2$ level is high despite the high SMC, because the very high levels of τ increase the emissivity. Here, the tau–omega model was also used to fit the geophysical relationship between $T_I/2$ and Γ_{rl}, as well as over croplands areas where it is expected to have a stronger coherent reflectivity $\langle |Y_{r,\mathrm{coh}}(\tau, f)|^2 \rangle$ because of the lower τ and surface roughness. Fig. 3(a) shows high SMC values $\sim 0.5\,\mathrm{m}^3/\mathrm{m}^3$ along the complete Γ_{rl} dynamic range, while $T_I/2$ appears saturated at $\sim[275, 280]$ K with τ values $\sim$1.15. Dense vegetation dominates the emissivity, while GNSS-R shows a larger dynamic range that could be associated with inland water bodies that could also explain the low $T_I/2$ dynamic range. The strong coherent scattering due to the significant number of rivers [70] is partially attenuated by the vegetation. This explains the large Γ_{rl} dynamic range in the region, despite nearly SMC values. τ is the dominant parameter over wet biomass (e.g., Amazon target area), with moderate ω values. Thus, it is expected a large signal attenuation and a lower impact of incoherent scattering effects.

Over Thailand, $T_I/2$ levels are higher as τ increases and SMC decreases [see Fig. 3(b), (e), and (h)]. However, τ dominates $T_I/2$ for levels higher than $\sim$270 K, in agreement with observations over the Amazon. At the same time, in this target area, there are reflectivity peaks $\Gamma_{rl} \sim [-5, -2]$ dB that could be associated with irrigated rice production, since $\Gamma_{rl} \sim -2$ dB corresponds to flat freshwater surfaces in agreement with the Fresnel reflectivity [28]. In this sense, the reflectivity peaks up to ~ -2 dB over the Amazon target area are also a symptom that there is a strong coherent scattering term $\langle |Y_{r,\mathrm{coh}}(\tau, f)|^2 \rangle$ nearly independent of the R_T (12).

Over the Argentinian Pampas [see Fig. 3(c), (f), and (i)], τ levels are low and quite homogeneous. It is clear how $T_I/2$ decreases while Γ_{rl} increases for higher SMC values with an apparent negligible saturation due to the vegetation. This indicates that SMC dominates Γ_{rl} for low opacity τ levels, because in this

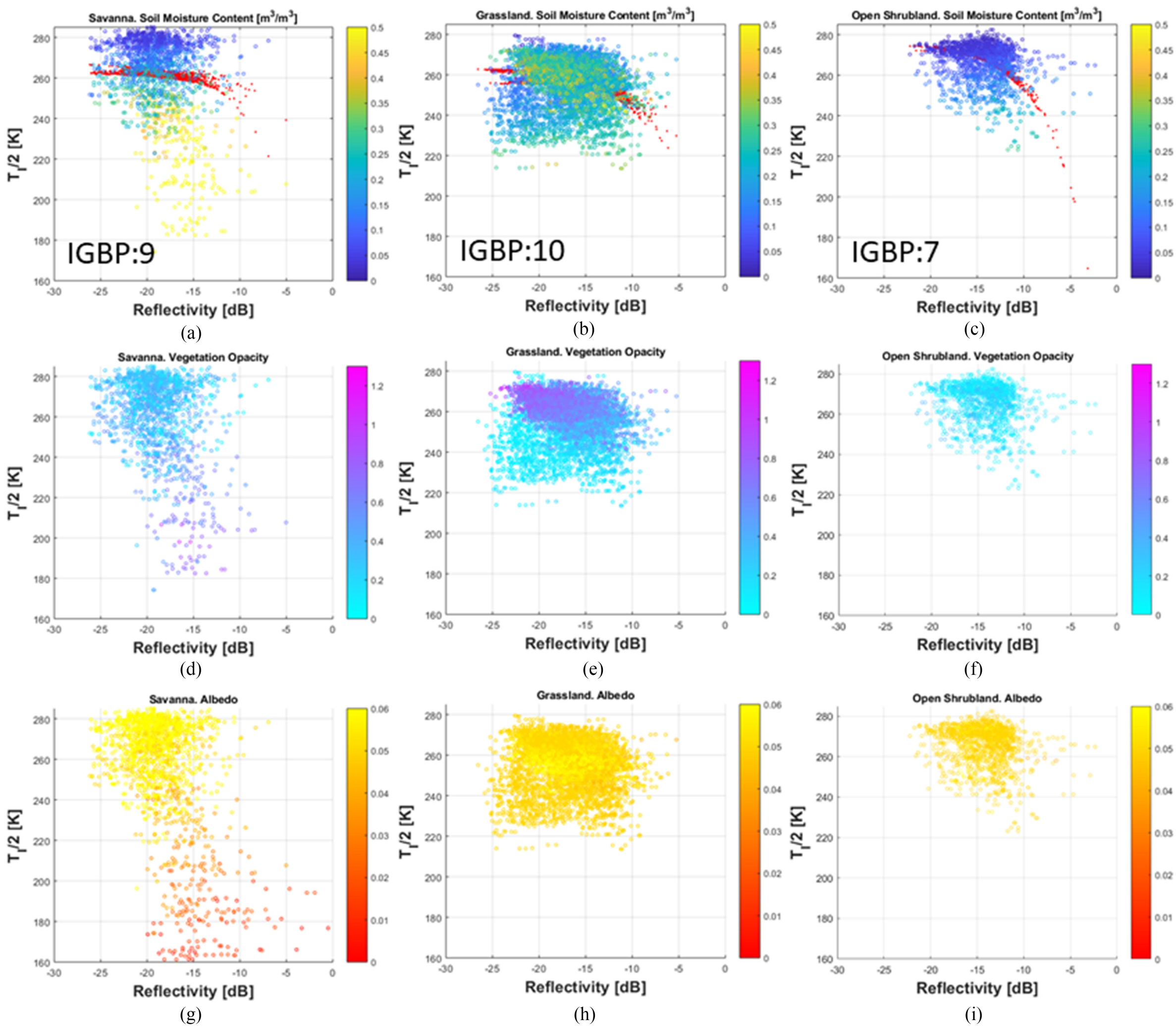

Fig. 4. Relationship between CyGNSS reflectivity Γ_{rl} and SMAP radiometer normalized brightness temperature $T_I/2$, as a function of (a)–(c) SMC, (d)–(f) vegetation opacity τ, and (g)–(i) albedo ω; and for different target areas (a), (d), (g) Tanzania, (b), (e), (h) US Midwest, and (c), (f), (i) Murrumbidgee. In (a)–(c), tau–omega model used to fit the scatter-plots is also depicted (red dots).

situation the GNSS signal penetration through the vegetation is high, and thus the coherent scattering mechanism associated with the soil is dominant.

B. Tanzania, US Midwest, and Murrumbidgee: Moderate SMC Levels

Fig. 4 shows the analysis over Tanzania [see Fig. 6(d)], US Midwest [see Fig. 6(e)], and Murrumbidgee [see Fig. 6(f)], with low-to-moderate SMC, high RVIs [$\mathrm{RVI}_{\mathrm{Tanzania}} \sim 0.8$, $\mathrm{RVI}_{\mathrm{USMidwest}} \sim 0.65$, and $\mathrm{RVI}_{\mathrm{Murrumbidgee}} \sim 0.69$], and high GSIs [$\mathrm{GSI}_{\mathrm{Tanzania}} \sim 0.72$, $\mathrm{GSI}_{\mathrm{USMidwest}} \sim 0.79$, and $\mathrm{GSI}_{\mathrm{Murrumbidgee}} \sim 0.43$]. The dominant IGBPs are grassland (IGBP 10), savanna (IGBP 9), and open shrubland (IGBP 7), respectively. Savannas are characterized by porous soils with a thin layer of humus. Seasonal heavy rains can drain quickly, preventing swampy conditions. The trees are widely spaced so that the canopy does not close. Open shrubland is covered by relatively dense foliage cover ~30%–70% and short trees; while the US-grassland's main biome are short-, mixed-, and tall-grass prairies [71]. These three selected target areas are characterized by low τ levels [see Fig. 4(d)–(f)]. Thus, as a first thought, $T_I/2$ and Γ_{rl} should be mainly linked to SMC.

Decreasing $T_I/2$ dynamic ranges [~ 100 K (Tanzania), ~ 60 K (US Midwest), ~ 40 K (Murrumbidgee)] correspond to decreasing SMC ranges [$< 0.5\,\mathrm{m}^3/\mathrm{m}^3$ (Tanzania), $< 0.3\,\mathrm{m}^3/\mathrm{m}^3$ (US Midwest), $< 0.1\,\mathrm{m}^3/\mathrm{m}^3$ (Murrumbidgee)] [see Fig. 4(a)–(c)]. The associated Pearson correlation coefficients are $r_{\mathrm{Tanzania}} \sim -0.49$, $r_{\mathrm{US}} \sim -0.25$, and $r_{\mathrm{Murrumbidgee}} \sim -0.12$. In Tanzania, Fig. 4(a) shows SMC peaks $\sim 0.5\,\mathrm{m}^3/\mathrm{m}^3$, and as expected, $T_I/2$ decreases. Thus, the $T_I/2$ dynamic range is larger; however, $\Gamma_{rl} \sim [-25, -10]$ dB is low [see Fig. 6(d)]. The interpretation is twofold: a) low surface-moisture levels associated with porous soils that decrease the surface reflectivity; b) higher vegetation scattering contribution ω [see Fig. 4(g)] belonging to a reduced signal coherence and an increment of incoherent scattering $\langle |Y_{r,\mathrm{incoh}}(\tau, f)|^2 \rangle$ that reduce the signal power returns. In addition to low SMC levels, the latter aspect is understood as a trigger of the lower reflectivity also in the US Midwest $\Gamma_{rl} \sim [-25, -10]$ dB and Murrumbidgee $\Gamma_{rl} \sim [-20, -10]$ dB.

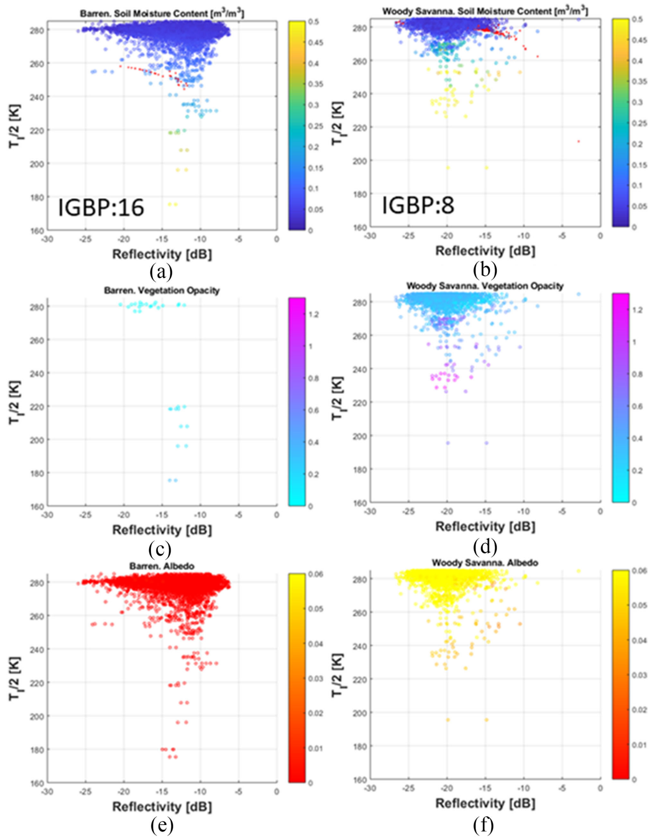

Fig. 5. Relationship between CyGNSS reflectivity Γ_{rl} and SMAP radiometer normalized brightness temperature $T_I/2$, as a function of (a), (b) SMC, (c), (d) vegetation opacity τ, and (e), (f) albedo ω; and for different target areas (a), (c), (e) Sahara desert, and (b), (d), (f) Northeast region of Brazil. In (a)–(b), tau-omega model used to fit the scatter-plots is also depicted (red dots).

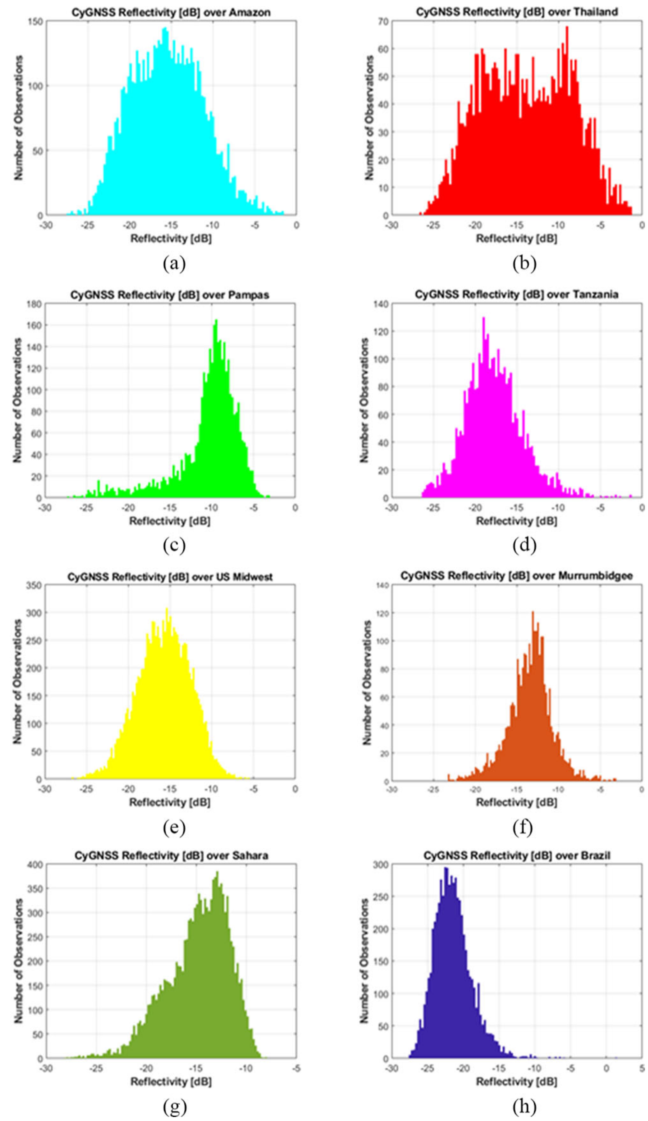

Fig. 6. Histrograms of the CyGNSS reflectivity Γ_{rl} over the selected target areas: (a) Amazon, (b) Thailand, (c) Argentinian Pampas, (d) Tanzania, (e) US Midwest, (f) Murrumbidgee, (g) Sahara, and (f) Northeast of Brazil.

Overall, the scatter plots of Fig. 4 show a higher dispersion of the measurements as compared with those in other regions (see Figs. 3–5). This aspect is linked to the impact of the land cover heterogeneity (high GSI levels) over the selected target areas (see Table II). Land heterogeneity is a critical aspect in geophysical parameter retrieval as an indication of diversity. In regions with larger vegetation gradients such as US Midwest [see Fig. 4(e)], the GSI impact could be even more amplified.

C. Sahara and Northeast Region of Brazil: Low SMC Levels

Fig. 5 shows the analysis over Sahara [see Fig. 6(g)] and the Northeast Region of Brazil [see Fig. 6(h)], with very low SMC, different RVIs [$\mathrm{RVI}_{\mathrm{Sahara}} \sim 0.12$, and $\mathrm{RVI}_{\mathrm{Northeast}} \sim 0.87$], and low GSIs [$\mathrm{GSI}_{\mathrm{Sahara}} \sim 0$, and $\mathrm{GSI}_{\mathrm{Northeast}} \sim 0.35$]. The dominant IGBPs are barren (IGBP 16) and woody savanna (IGBP 8), respectively. The Sahara is covered by rocky mountains, boulder and graves zones, and shifting sand dunes ("sand seas"); with almost negligible vegetation. In addition to surface scattering, DDMs $\langle |Y_r(\tau,f)|^2\rangle$ could have a contribution of volumetric scattering over areas with rich sand content and with very dry conditions, since the penetration depth at L-band is around ∼2 m for 0% of volumetric moisture [72]. On the other hand, woody savanna is characterized by dry forests, including: a) "low shrubby *caatinga"* (<1 m of canopy height) associated with shallow sandy soils and gently undulating surface, and b) "tall *caatinga* forest" (<25 m of canopy height) associated with eutrophic soils derived from basic rocks. Scattering albedo ω is especially sensitive to woody biomass [66].

The $T_I/2$ dynamic range over the Sahara Desert is very small, as expected over a very dry region with negligible vegetation. Thus, there is no correlation between both types of sensors (see Fig. 5). On the other hand, the Γ_{rl} range is wide $\sim[-25-7]$ dB, with relatively high-power returns. This could be attributed to subsurface effects (not considered in our model) that increase the power of the reflected signals, and the long-term wind that continuously reshapes the surface. This introduces a temporal variation of the bistatic scattering coefficient σ^0, explaining the significant Γ_{rl} dynamic range ∼18 dB.

Over the Northeast Region of Brazil [see Fig. 5(b), (d), and (f)], the Γ_{rl} range $\sim [-27-15]$ dB is smaller as compared with Sahara [see Fig. 5(a), (c), and (e)]. The almost negligible

This article has been accepted for inclusion in a future issue of this journal. Content is final as presented, with the exception of pagination.

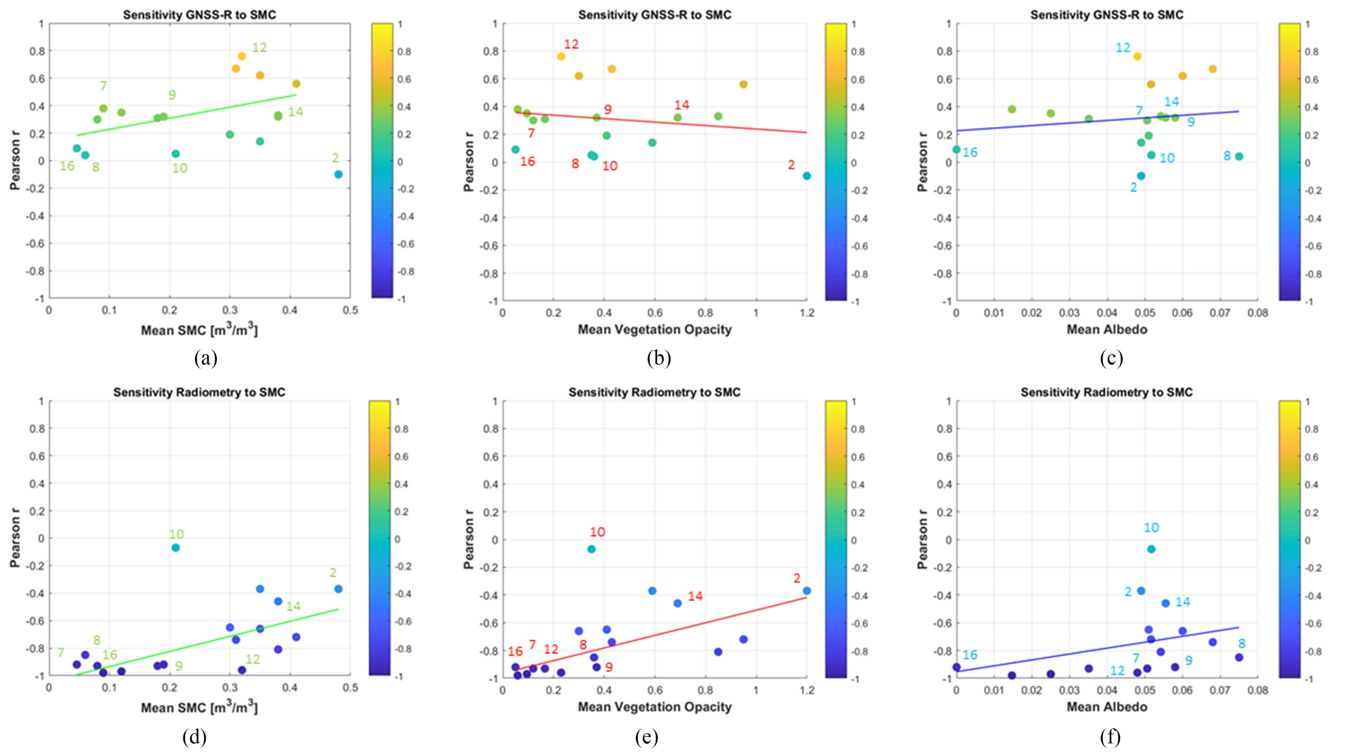

Fig. 7. Scatter plot of Pearson coefficients r_Γ_{rl} (a)–(c) and $r\_T_I/2$ (d)–(f) and robust fits versus SMC, for different mean values of SMC (a), (d), τ (b), (e), and ω (c), (f). See Table I for detailed information of the IGBP number marked with dots.

SMC [see Fig. 5(b)], and the high levels of vegetation scattering ω [see Fig. 5(f)] explain the low Γ_{rl}, while showing a significant dynamic range ∼10 dB. Because of the lack of $T_I/2$ dynamic range, the slope between $T_I/2$ and Γ_{rl} is almost zero. As a final remark of this region, it appears a reduced dispersion of the measurements as compared with regions with moderate and diverse SMC levels, despite a higher structural effects (RVI $\sim$ 0.87). The impact of a low/very low SMC level is to reduce the power levels of the soil-scattered signals, but also explains the near constants high $T_I/2$ level.

V. Parametric Sensitivity Assessment of GNSS-R and Radiometry

Passive microwave measurements have the potential to estimate SMC, τ, and ω. L-band missions such as SMAP, SMOS, and Aquarius are more sensitive to lower canopy layers than optical sensors, and thus they can accurately estimate τ effects on the radiometer measurements to provide accurate SMC. This approach assumes that τ changes more slowly than SMC and that it is nearly constant over adjacent overpasses.

Here, the sensitivity changes of GNSS-R and microwave radiometry to these geophysical parameters were assessed. The fluctuations of the Pearson coefficients of Γ_{rl} (r_Γ_{rl}) and $T_I/2$ ($r\_T_I/2$) versus SMC (see Fig. 7), τ (see Fig. 8), and ω (see Fig. 9) were studied as a function of the mean values of SMC [see Figs. 7–9(a) and (d)], τ [see Figs. 7–9(b) and (e)], and ω [see Figs. 7–9(c) and (f)] over the selected target areas. In the interpretation of these results (see Table III) it is worth noting that the SMAP's antenna gain is ∼36 dB [26], while that of CyGNSS is ∼14.5 dB [24]. The GNSS-R sensitivity to SMC increases for higher SMC [see Fig. 7(a)], while the radiometric sensitivity to SMC decreases [Fig. 7(d)]. CyGNSS-based GNSS-R improves the sensitivity as $\sim 0.85/(\mathrm{m}^3/\mathrm{m}^3)$ [see Fig. 7(a)], while SMAP-based radiometry losses the sensitivity as $\sim 1.25/(\mathrm{m}^3/\mathrm{m}^3)$ [see Fig. 7(d)]. A future study from a GNSS-R platform with a higher antenna gain should be performed to investigate the achievable sensitivity to SMC and polarimetric ratio should be used to cancel out the surface roughness effects on σ^0 [20]. However, the sensitivity of the SMAP-based microwave radiometry for low SMC is very high, with a Pearson coefficient that tends to ∼0.9. On the other hand, both types of sensors reduces the sensitivity to SMC as larger are the effects of vegetation attenuation τ [see Fig. 7(b) and (e)]. The effect of signal attenuation is more pronounced than that of vegetation scattering [see Fig. 7(b), (c), (e), and (f) and Table III]. In particular, GNSS-R losses sensitivity as $\sim 0.36/(1\,\tau\,\mathrm{unit})$ [see Fig. 7(b)], while radiometry as $\sim$ $0.54/(1\,\tau\,\mathrm{unit})$ [see Fig. 7(e)].

The GNSS-R and radiometric sensitivities to changes on τ (see Fig. 8) decrease for increasing values of SMC $\sim [0, 0.25]\,\mathrm{m}^3/\mathrm{m}^3, \tau \sim$ $[0, 0.2 - 0.3]$, and ω $\sim [0, 0.04 - 0.05]$; while there is a change of trend for larger values of these parameters SMC $\sim [0.25, 0.5]\,\mathrm{m}^3/\mathrm{m}^3, \tau \sim [0.2 - 0.3\,1.2]$, and $\omega \sim [0.04 - 0.05\,0.08]$. In the first range, the Pearson coefficients are positive for GNSS-R $r_{\mathrm{GNSS-R}} > 0$, and negative for microwave radiometry $r_{\mathrm{Rad}} < 0$. Two main explanations are found that justify these empirical observations: a) Γ_{rl} increases with increasing τ values, because they are mostly associated

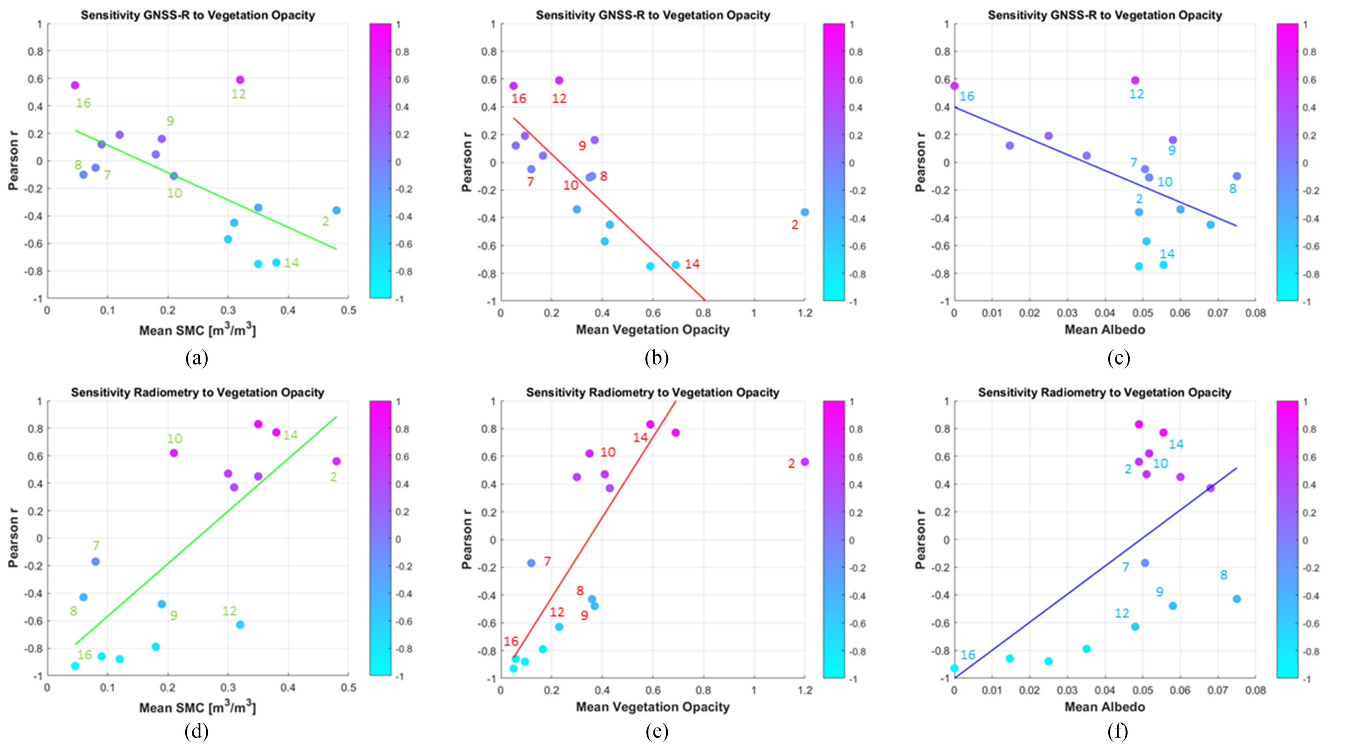

Fig. 8. Scatter plot of r_Γ_{rl} (a)–(c) and $r\_T_I/2$ (d)–(f) and robust fits versus τ, for different mean values of SMC (a), (d), τ (b), (e), and ω (c), (f). See Table I for detailed information of the IGBP number marked with dots.

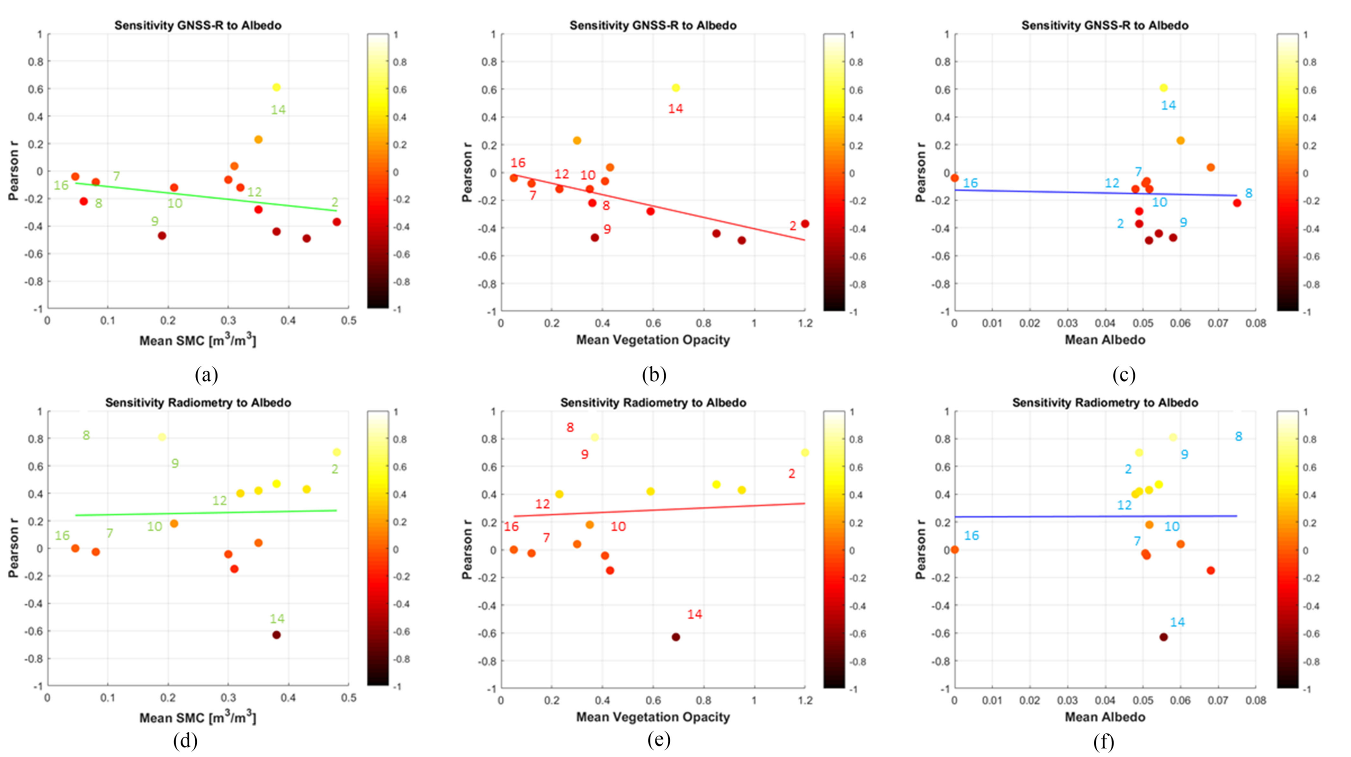

Fig. 9. Scatter plot of r_Γ_{rl} (a)–(c) and $r\_T_I/2$ (d)–(f) and robust fits versus ω, for different mean values of SMC (a), (d), τ (b), (e), and ω (c), (f). See Table I for detailed information of the IGBP number marked with dots.

TABLE III
PEARSON LINEAR CORRELATION COEFFICIENT OF THE PEARSON COEFFICIENTS OF r_Γ_{rl} AND $r\_T_I/2$ VERSUS SMC, τ AND ω FOR DIFFERENT MEAN VALUES OF THESE PARAMETERS OVER THE SPECIFIC TARGET AREAS

Pearson	SMC	τ	ω
Γ_{rl} vs SMC	0.48	-0.19	0.14
$T_I/2$ vs SMC	0.52	0.52	0.32
Γ_{rl} vs τ	-0.60	-0.62	-0.53
$T_I/2$ vs τ	0.75	0.70	0.58
Γ_{rl} vs ω	-0.03	-0.32	0
$T_I/2$ vs ω	-0.08	0.23	0.22

to increasing values of SMC, as one can expect over areas with little vegetation; b) $T_I/2$ is mostly associated with the soil surface, so that an increment in SMC reduces the emissivity. This range of parameters cover a significant fraction of the Earth's surface where microwave radiometry SMC accuracy requirements $(0.04\,\mathrm{m}^3/\mathrm{m}^3)$ can be met [64, Fig. 6]. In the second range, there is a change of trend belonging to an inverse behaviour $r_{\mathrm{GNSS-R}} < 0$ and $r_{\mathrm{Rad}} > 0$. In this case, the interpretation is also twofold: a) here the attenuation is high, and thus Γ_{rl} decreases despite the high SMC; b) the vegetation emission contributes significantly to the radiometer measurements. Fig. 9 shows $T_I/2$ measurements without appreciable sensitivity to ω, and at the same time, increasing anticorrelation of Γ_{rl} and ω as larger is τ.

VI. SUMMARY AND CONCLUSION

In this paper, the impact of SMC, τ, and ω on the relationship between CyGNSS GNSS-R bistatic reflectivity Γ_{rl} and SMAP microwave radiometry brightness temperature $T_I/2$ has been quantified as a function of the dominant IGBP land cover type, the RVI, and GSI indices. The tau–omega model was used to fit this geophysical relationship over the selected target areas, with the following Pearson coefficients between Γ_{rl} and $T_I/2$: $r_{\mathrm{Thailand}} \sim -0.87$, $r_{\mathrm{Pampas}} \sim -0.7$, $r_{\mathrm{Tanzania}} \sim -0.49$, $r_{\mathrm{Amazon}} \sim -0.26$, $r_{\mathrm{US}} \sim -0.25$, $r_{\mathrm{Murrumbidgee}} \sim -0.12$, $r_{\mathrm{Northeast}} \sim -0.09$, and $r_{\mathrm{Sahara}} \sim -0.06$. The correlation between both types of sensors increases for higher SMC, and a more homogeneous vegetation cover type (lower GSIs). This correlation is especially high over croplands (IGBPs 12 and 14), which opens several possibilities to improve hydrological and agricultural monitoring taking advantage of the following properties: a) the good accuracy of microwave radiometry and the better spatial resolution of GNSS-R, and b) the high spatio-temporal sampling of a space-borne GNSS-R sensor. Then, an intercomparison between the sensitivity of GNSS-R and microwave radiometry to SMC, τ, and ω has been performed as a function of the mean values of these parameters over the selected target areas. Overall, it appears that: a) the GNSS-R sensitivity to SMC is more affected by SMC than τ and ω; while in the case of microwave radiometry both, τ and ω, have a more pronounced effect as compared with GNSS-R; and b) GNSS-R sensitivities to τ are lower than those corresponding to microwave radiometry.

As higher is the SMC, the sensitivity of CyGNSS reflectometer (antenna gain ∼14.5 dB) increases, while that of SMAP radiometer (antenna gain ∼36 dB) decreases. While microwave radiometry has a limitation associated with the physics behind the measurements, GNSS-R sensitivity could be improved by means of a higher antenna gain. On the other hand, observations show that GNSS-R is less affected by the wet biomass (τ). Thus, further research work with an improved antenna gain in future GNSS-R experiments could provide useful information to elucidate the regimes under which the different information provided by both techniques could be optimally used.

REFERENCES

[1] A. Camps, "Application of interferometric radiometry to Earth observation," Ph.D. Dissertation, Dept. Signal Theory Commun., Universitat Politècnica de Catalunya, Barcelona, Spain, 1996. [Online]. Available: http://www.tdx.cat/handle/10803/6885. Accessed on: Mar. 01, 2018.
[2] Y. H. Kerr, P. Waldteufel, J. P. Wigneron, J. Martinuzzi, J. Font, and M. Berger, "Soil moisture retrieval from space: The soil moisture and ocean salinity (SMOS) mission," *IEEE Trans. Geosci. Remote Sens.*, vol. 39, no. 8, pp. 1729–1735, Aug. 2001.
[3] K. Kellogg *et al.*, "NASA's soil moisture active passive (SMAP) observatory," in *Proc. IEEE Aerosp. Conf.*, Big Sky, MT, USA, 2003, pp. 1–20.
[4] D. Entekhabi *et al.*, "The soil moisture active/passive mission (SMAP)," in *Proc. IEEE Int. Geosci. Remote Sens. Symp.*, Boston, MA, USA, Jul. 2008, pp. III 1–III 4.
[5] M. F. P. Bierkens *et al.*, "Hyper-resolution global hydrological modelling: What is next? Everywhere and locally relevant," *Hydrol. Process.*, vol. 29, pp. 310–320, Dec. 2014.
[6] M. Martín-Neira, "A passive reflectometry and interferometry system (PARIS): Application to ocean altimetry," *ESA J.*, vol. 17, pp. 331–355, Jan. 1993.
[7] S. T. Lowe, J. L. LaBrecque, C. Zuffada, L. J. Romans, L. E. Young, and G. A. Hajj, "First spaceborne observation of an earth-reflected GPS signal," *Radio Sci.*, vol. 37, no. 1, pp. 7-1–7-28, 2002.
[8] V. U. Zavorotny, S. Gleason, E. Cardellach, and A. Camps, "Tutorial on remote sensing using GNSS bistatic radar of opportunity," *IEEE Geosci. Remote Sens. Mag.*, vol. 2, no. 4, pp. 8–45, Dec. 2014.
[9] E. Cardellach *et al.*, "GNSS transpolar earth reflectometry exploring system (G-TERN): Mission concept," *IEEE Trans. Geosci. Remote Sens.*, vol. 6, pp. 13980–14018, Mar. 2018.
[10] A. Egido *et al.*, "Airborne GNSS-R polarimetric measurements for soil moisture and above-ground biomass estimation," *IEEE J. Sel. Top. Appl. Earth Obs. Remote Sens.*, vol. 7, no. 5, pp. 1522–15320, May 2014.
[11] N. Pierdicca, L. Guerriero, R. Giusto, M. Brogioni, and A. Egido, "SAVERS: A simulator of GNSS reflections from bare and vegetated soils," *IEEE Trans. Geosci. Remote Sens.*, vol. 52, no. 10, pp. 6542–6554, Oct. 2014.
[12] H. Carreno-Luengo, A. Amèzaga, D. Vidal, R., Olivé, J. F. Munoz, and A. Camps, "First polarimetric GNSS-R measurements from a stratospheric flight over boreal forests," *MDPI Remote Sens.*, vol. 7, no. 10, pp. 13120–13138, Oct. 2015.
[13] E. Motte *et al.*, "GLORI: A GNSS-R dual polarization airborne instrument for land surface monitoring," *MDPI Sensors*, vol. 16. no. 5, May 2016, Art. no. 732.
[14] M. Martín-Neira, S. D'Addio, C. Buck, N. Floury, and R. Prieto-Cerdeira, "The PARIS ocean altimeter in-orbit demonstrator," *IEEE Trans. Geosci. Remote Sens.*, vol. 49, no. 6, pp. 2209–2237, Jun. 2011.
[15] E. Cardellach *et al.*, "Consolidating the precision of interferometric GNSS-R ocean altimetry using airborne experimental data," *IEEE Trans. Geosci. Remote Sens.*, vol. 52, no. 5, pp. 4992–5004, Aug. 2014.
[16] J. Wickert *et al.*, "GEROS-ISS: GNSS reflectometry, radio occultation, and scatterometry on-board the international space station," *IEEE J. Sel. Top Appl. Earth Observ. Remote Sens.*, vol. 9, no. 10, pp. 4552–4581, Oct. 2016.

[17] M. Unwin, P. Jales, J. Tye, C. Gommenginger, G. Foti, and J. Rose, "Spaceborne GNSS-reflectometry on TechDemoSat-1: Early mission operations and exploitation," *IEEE J. Sel. Top. Appl. Earth Observ. Remote Sens.*, vol. 9, no. 10, pp. 4525–4539, Apr. 2014.

[18] R. Rose, W. Wells, D. Rose, C. Ruf, A. Ridley, and K. Nave, "Nanosat technology and managed risk: An update of the CyGNSS microsatellite constellation mission development," in *Proc. 28th AIAA/USU Conf. Small Satell.*, Logan, UT, USA, Aug. 2014, pp. 1–12.

[19] C. Ruf, S. Gleason, A. Ridley, R. Rose, and J. Scherrer, "The NASA CyGNSS mission: Overview and status update," in *Proc. IEEE Int. Geosci. Remote Sens. Symp.*, Fort Worth, TX, USA, Jul. 2018, pp. 2641–2643.

[20] H. Carreno-Luengo, S. Lowe, C. Zuffada, S. Esterhuizen, and S. Oveisgharan, "Spaceborne GNSS-R from the SMAP mission: First assessment of polarimetric scatterometry over land and cryosphere," *MDPI Remote Sens.*, vol. 9. no. 361, Apr. 2017, Art. no. 362.

[21] C. Chew *et al.*, "SMAP radar receiver measures land surface freeze/thaw state through capture of forward-scattered L-band signals," *Remote Sens. Environ.*, vol. 198, no. 1, pp. 333–344, Sep. 2017.

[22] CYGNSS. 2017. CYGNSS Level 1 Science Data Record Version 2.0. Ver. 2.0. PO.DAAC, CA, USA. [Online]. Available http://dx.doi.org/10.5067/CYGNS-L1X20. Accessed on: Jan. 05, 2018.

[23] C. Ruf *et al.*, "New ocean winds satellite mission to probe hurricanes and tropical convection," *Bull. Amer. Meteorol. Soc.*, vol. 97, pp. 385–395, 2015, doi: 10.1175/BAMS-D-14-00218.1.

[24] C. Ruf *et al.*, "CyGNSS handbook. Cyclone global navigation satellite systems," [Online]. Available http://clasp-research.engin.umich.edu/missions/cygnss/reference-material.php. Accessed on: Jan. 04, 2018.

[25] P. E. O'Neill, S. Chan, E. G. Njoku, T. Jackson, and R. Bindlish, SMAP Enhanced L3 Radiometer Global Daily 9 km EASE-Grid Soil Moisture, Version 1. [SPL3SMP_E]. Boulder, CO, USA: NASA Nat. Snow Ice Data Center Distrib. Active Archive Center, 2016. [Online]. Available https://doi.org/10.5067/ZRO7EXJ8O3XI. Accessed on: Jan. 05, 2018.

[26] D. Entekhabi *et al.*, "SMAP handbook. Soil moisture active passive," [Online]. Available https://nsidc.org/data/SPL3SMP_E/versions/1. Accessed on: Jun. 04, 2018.

[27] W. Peake, "Interaction of electromagnetic waves with some natural surfaces," *IEEE Trans. Antennas Propag.*, vol. AP-7, no. 1, pp. 324–329, Dec. 1959.

[28] F. T. Ulaby and D. G. Long, *Microwave Radar and Radiometric Remote Sensing*, Univ. Michigan Press: Ann Arbor, MI, USA, 2014, pp. 252.

[29] A. Camps *et al.*, "The WISE 2000 and 2001 field experiments in support of the SMOS mission: Sea surface L-band brightness temperature observations and their application to sea surface salinity retrieval," *IEEE Trans. Geosci. Remote Sens.*, vol. 42, no. 4, pp. 804–823, Apr. 2004.

[30] L. Tsang and R. W. Newton, "Microwave emissions from soils with rough surfaces," *J. Geophys. Res.*, vol. 87, no. 11, pp. 9017–9024, Oct. 1982.

[31] M. Martin-Neira, W. Li, A. Andres-Beivide, and X. Ballesteros-Sels, "Cookie: A satellite concept for GNSS remote sensing constellations," *IEEE J. Sel. Top. Appl. Earth Observ. Remote Sens.*, vol. 9, no. 10, pp. 4593–4610, Oct. 2016.

[32] H. Carreno-Luengo and A. Camps, "Empirical results of a surface-level GNSS-R experiment in a wave channel," *MDPI Remote Sens.*, vol. 7, pp. 7471–7493, Jun. 2015.

[33] H. Carreno-Luengo, A. Camps, J. Querol, and G. Forte, "First results of a GNSS-R experiment from a stratospheric balloon over boreal forests," *IEEE Trans. Geosci. Remote Sens.*, vol. 54, no. 5, pp. 2652–2663, Dec. 2015.

[34] W. Li, E. Cardellach, F. Fabra, A. Rius, S. Ribó, and M. Martín-Neira, "First spaceborne phase altimetry over sea ice using TechDemoSat-1 GNSS-R signals," *Geophys. Res. Lett.*, vol. 44, no. 16, pp. 8369–8376, Aug. 2017.

[35] E. G. Njoku and J. A. Kong, "Theory for passive microwave remote sensing of near surface soil moisture," *J. Geophys. Res.*, vol. 82, pp. 3108–3118, 1977.

[36] V. U. Zavorotny and A. G. Voronovich, "Scattering of GPS signals from the ocean with wind remote sensing application," *IEEE Trans. Geosci. Remote Sens.*, vol. 38, no. 2, pp. 951–964, Mar. 2000.

[37] A. G. Voronovich and V. U. Zavorotny, "Bistatic radar equation for signals of opportunity revisited," *Trans. Geosci. Remote Sens.*, vol. 56, no. 4, pp. 1959–1968, Dec. 2017.

[38] R. D. De Roo and F. T. Ulaby, "Bistatic specular scattering from rough dielectric surfaces," *IEEE Trans. Antennas Propag.*, vol. 42, no. 2, pp. 220–231, Feb. 1994.

[39] D. Masters, P. Axelrad, and S. Katzberg, "Initial results of land-reflected GPS bistatic radar measurements in SMEX02," *Remote Sens. Environ.*, vol. 92. no. 4, pp. 507–520, Sep. 2002.

[40] N. Pierdicca, L. Guerriero, M. Brogioni, and A. Egido, "On the coherent and non-coherent components of bare and vegetated terrain bistatic scattering: Modelling the GNSS-R signal over land," in *Proc. IEEE Int. Geosci. Remote Sens. Symp.*, Munich, Germany, Jul. 2017, pp. 3407–3410.

[41] H. Carreno-Luengo and A. Camps, "Unified GNSS-R formulation including coherent and incoherent scattering components," in *Proc. IEEE Int. Geosci. Remote Sens. Symp.*, Beijing, China, Jul. 2016, pp. 4815–4816.

[42] S. Gleason, "Remote sensing of ocean, ice and land surfaces using bistatically scattered GNSS signals from low earth orbit," Ph.D. dissertation, Univ. Surrey, Surrey, U.K., 2006. Accessed on: Mar. 01, 2018.

[43] S. Chandraskhar, *Radiative Transfer*. New York, NY, USA: Dover Publications Inc., 1960.

[44] Y. H. Kerr *et al.*, "The SMOS soil moisture retrieval algorithm," *IEEE Trans. Geosci. Remote Sens.*, vol. 50, no. 5, pp. 1384–1403, May 2012.

[45] Array Systems Computing Inc., Algorithm theoretical basis document (ATBD) for the SMOS Level 2 soil moisture processor development continuation project, ref SO-TN-ARR-L2PP-0037, no. 3.3, 2010. [Online]. Available https://earth.esa.int/pub/ESA_DOC/SOTN-ARR-L2PP-0037_ATBD_v3_3.pdf. Accessed on: Jan. 02, 2018.

[46] S. Paloscia and P. Pampaloni, "Microwave polarization index for monitoring vegetation growth," *IEEE Trans. Geosci. Remote Sens.*, vol. 26, no. 5, pp. 617–621, Sep. 1988.

[47] W. H. McMaster, "Polarization and the stokes parameters," *Amer. J. Phys.*, vol. 22, no. 6, 1954, Art. no. 351.

[48] A. Alonso-Arroyo *et al.*, "On the correlation between GNSS-R reflectivity and L-band microwave radiometry," *IEEE J. Sel. Top. Appl. Earth Observ. Remote Sens.*, vol. 9, no. 12, pp. 5862–5879, Apr. 2016.

[49] S. Gleason, C. Ruf, M.-P. Clarizia, and A. J. O'Brien, "Calibration and unwrapping of the normalized scattering cross section for the cyclone global navigation satellite system," *IEEE Trans. Geosci. Remote Sens.*, vol. 54, no. 5, pp. 2495–2509, Jan. 2016.

[50] M. Unwin, P. Jales, P. Blunt, S. Duncan, M. Brummitt, and C. Ruf, "The SGR-ReSI and its application for GNSS reflectometry on the NASA EV-2 CYGNSS mission," in *Proc. IEEE Aerosp. Conf.*, Big Sky, MT, USA, May 2013, pp. 1–6.

[51] S. Gleason and C. Ruf, "Overview of the delay Doppler mapping instrument (DDMI) for the cyclone global navigation satellite systems mission (CYGNSS)," in *Proc. IEEE MTT-S Int. Microw. Symp.*, Phoenix, AZ, USA, May 2015, pp. 1–3.

[52] E. Cardellach, "Sea surface determination using GNSS reflected signals," Ph.D. dissertation, Universitat Politècnica de Catalunya, Barcelona, Spain, 2001. [Online]. Available view_theses.php?TID=2 view_theses.php?TID=2. Accessed on: Apr. 16, 2018.

[53] S. K. Chan *et al.*, "Development and assessment of the SMAP enhanced passive soil moisture product," *Remote Sens. Environ.*, vol. 204, pp. 931–941, Jan. 2018.

[54] P. O'Neill, S. Chan, E. Njoku, T. Jackson, and R. Bindlish, "Soil moisture active passive (SMAP) algorithm theoretical basis document level 2 & 3 soil moisture (passive) data products. Revision C," Dec. 2016. [Online]. Available https://nsidc.org/data/SPL3SMP_E/versions/1. Accessed on: Apr. 16, 2018.

[55] C. D. Bussy-Virat, C. S. Ruf, and A. J. Ridley, "Relationship between temporal and spatial resolution for a constellation of GNSS-R satellites," *IEEE J. Sel. Top. Appl. Earth Observ. Remote Sens.*, vol. PP, no. 99, pp. 1–10, May 2008, doi: 10.1109/JSTARS.2018.2833426.

[56] MODIS, MCD12Q1, Version 5. NASA EOSDIS Land Processes DAAC, USGS Earth Resources Observation and Science (EROS) Center, Sioux Falls, South Dakota, 2011. [Online]. Available https://lpdaac.usgs.gov. Accessed on: Jun. 04, 2018.

[57] Y. Kim and J. van Zyl, "On the relationship between polarimetric parameters," in *Proc. IEEE Int. Geosci. Remote Sens. Symp.*, Honolulu, HI, USA, Jul. 2000, pp. 1298–1300.

[58] M. Arii, J. van Zyl, and Y. Kim, "A general characterization for polarimetric scattering from vegetation canopies," *IEEE Trans. Geosci. Remote Sens.*, vol. 48, no. 9, pp. 3349–3357, May 2010.

[59] K. A. McColl, D. Entekhabi, and M. Piles, "Uncertainty analysis of soil moisture and vegetation indices using Aquarius scatterometer observations," *IEEE Trans. Geosci. Remote Sens.*, vol. 52, no. 7, pp. 4259–4272, Jul. 2014.

[60] E. H. Simpson, "The measurement of diversity," *Nature*, vol. 163, no. 688, pp. 163–168, Apr. 1949.

[61] M. Piles, K. A. McColl, D. Entekhabi, N. Das, and M. Pablos, "Sensitivity of aquarius active and passive measurements temporal covariability to land surface characteristics," *IEEE Trans. Geosci. Remote Sens.*, vol. 53, no. 8, pp. 4700–4711, Aug. 2015.

[62] S. H. Yueh. *Aquarius CAP Level 2 Sea Surface Salinity, Wind Speed & Direction Data V4.0. Ver. 4.0. PO.DAAC*, CA, USA, 2015. [Online]. Available http://dx.doi.org/10.5067/AQR40-2TOCS. Accessed on: Jan. 05, 2018.

[63] S. H. Yueh, W. Tang, A. K. Hayashi, and G. S. E. Lagerloef, "L-band passive and active microwave geophysical model functions of ocean surface winds and applications to aquarius retrieval," *IEEE Trans. Geosci. Remote Sens.*, vol. 51, no. 9, pp. 4619–4632, Jul. 2013.

[64] A. Camps *et al.*, "Sensitivity of GNSS-R spaceborne observations to soil moisture and vegetation," *IEEE J. Sel. Top. Appl. Earth Observ. Remote Sens.*, vol. 9, no. 10, pp. 4730–4732, Oct. 2016.

[65] A. K. Konings, M. Piles, N. Das, and D. Entekhabi, "L-band vegetation optical depth and effective scattering albedo estimation from SMAP," *Remote Sens. Environ.*, vol. 198, pp. 460–470, Sep. 2017.

[66] Dryland and dryland with forests. [Online]. Available https://earthobservatory.nasa.gov/IOTD/view.php?id=90635. Accessed Jan. 02, 2018.

[67] M. T. Hallikainen, F. T. Ulaby, M. C. Dobson, M. A. Elrayes, and L. K. Wu, "Microwave dielectric behavior of wet soil-part 1: Empirical-models and experimental-observations," *IEEE Trans. Geosci. Remote Sens.*, vol. GRS-23, no. 1, pp. 25–34, Jan. 1985.

[68] L. Guerriero, P. Ferrazzoli, C. Vittucci, R. Rashmoune, M. Aurizzi, and A. Mattioni, "L-band passive and active signatures of vegetated soil: Simulations with a unified model," *IEEE J. Sel. Top. Appl. Earth Observ. Remote Sens.*, vol. 9, no. 6, pp. 2520–2531, Apr. 2016.

[69] N. N. Das, D. Entekhabi, E. G. Njoku, J. J. C. Shi, J. T. Johnson, and A. Colliander, "Tests of the SMAP combined radar and radiometer algorithm using airborne field campaign observations and simulated data," *IEEE Trans. Geosci. Remote Sens.*, vol. 52, no. 4, pp. 2018–2028, Apr. 2014.

[70] Hydrological data and maps based on SHuttle Elevation Derivatives at multiple Scales (HydroSEDS) Database. [Online]. Available https://hydrosheds.cr.usgs.gov/#. Accessed on: Jan. 02, 2018.

[71] J. R. Carpenter, "The grassland biome," *Ecological Monogr.*, vol. 10, no. 4, pp. 620–684, Oct. 1940.

[72] S. Xiong, J.-P. Muller, and G. Li, "The application of ALOS/PALSAR InSAR to measure subsurface penetration depths in deserts," *MDPI Remote Sens.*, vol. 9, no. 638, pp. 1–19, Jun. 2017.

Hugo Carreno-Luengo (S'12–M'14) received the degree in aeronautics engineering ("bachelor + master," Specialization in Spacecrafts) from the Escuela Técnica Superior de Ingenieros Aeronáuticos, the Universidad Politécnica de Madrid, Madrid, Spain, in 2010 and the Ph.D. degree (*cum laude*) from the Department of Physics, the Universitat Politècnica de Catalunya (UPC), Barcelona, Spain, 2016.

From 2009 to 2010, he performed the final degree project at the Department of Aircrafts and Space Vehicles. In 2011, he performed the Master of Space Science and Technology at the UPC. From 2012 to 2015, he was the Principal Investigator (PI) of the TORMES and TORMES 2.0 projects within ESA's REXUS/BEXUS and a co-PI in the E-GEM FP7 project. From 2013 to 2014, he was a Visiting Researcher with ESA-ESTEC, DLR, Esrange Space Center, and in Summer 2016, he was invited by the China Great Wall Industry Coorporation to assist the launch campaign of the ^{3}Cat-2 CubeSat at Jiuquan Satellite Launch Center. His research interests include the use of GNSS-R techniques to perform Earth remote sensing from nanosatellites.

Dr. Carreno-Luengo was a Session Chair at the 2015, 2017, and 2018 IEEE International Geoscience and Remote Sensing Symposium, and he has been the member of the IEEE GRSS since 2017. He was the recipient of the Predoctoral Fellowship by the Institut d'Estudis Espacials de Catalunya, and the NASA's Jet Propulsion Laboratory fellowship for a postdoctoral position (2016–2017) at Pasadena, CA, USA, in 2016. He was the recipient of the first position of the "Juan de la Cierva" research program, and of an IEEE GRSS award for the best Ph.D. thesis in geoscience and remote sensing, in 2017.

Guido Luzi received the Graduate degree in physics and the Ph.D. degree in electronic systems engineering from the University of Firenze, Firenze, Italy, in 1986 and 2000, respectively.

He has been working since 1986 in microwave remote sensing, active and passive, both in industrial and research institutions, dedicating his work to the development and experimentation of microwave sensors. He worked with the Department of Electronics and Telecommunications and the Department of Earth Sciences, University of Florence, working on various applications from monitoring volcanic areas as the Stromboli Island, to the development and experimentation of microwave sensors for the detection of vital signs (heart beat and breath), or civil engineering and cultural heritage applications. He moved to the Institute of Geomatics in 2010, where he was involved in the design and experimentation of radar-based sensing techniques with emphasis on ground-based synthetic aperture radar interferometry. He has authored or coauthored many papers in international journals concerning the aforementioned topics, and more than 50 papers in referred international journals. He has been with the Remote Sensing Department (Geomatics Division), Centre Tecnologic de Tele- 'comunicacions de Catalunya, Barcelona, Spain, since January 2014, where he is involved in research activities concerning the application of spaceborne and terrestrial radar techniques. His research interests include geophysical applications, with emphasis in the observation of landslides through terrestrial and satellite microwave interferometry and civil structures monitoring.

Dr. Luzi was the recipient of the international remote sensing campaigns, such as AGRISCATT87, AGRISCATT88, MACEurope, EPOCH, MEDALUS II, ENVIRONMENT, GALAHAD, and several national research contracts. He acts as a Referee for different journals IEEE TRANSACTIONS ON GEOSCIENCE AND REMOTE SENSING, IEEE GEOSCIENCE REMOTE SENSING LETTERS, *International Journal of Remote Sensing*, and IEEE SELECTED TOPICS IN APPLIED EARTH OBSERVATIONS.

Michele Crosetto received the civil engineering degree from the Politecnico di Torino, Turin, Italy, in 1993, and the doctorate degree in geodesy from the Politecnico di Milano, Milan, Italy, in 1998.

He specialized in geomatics in Lausanne (EPFL) and Zurich (ETHZ) from 1993 to 1995. He has worked with the Joint Research Centre of EC in Ispra, Italy (1999–2000) and at the Cartographic Institute of Catalonia in 2001. He has formed part of the Institute of Geomatics since 2002. Since January 2014, he is with CTTC, where he is currently the Head of the Geomatics Division. From the application point of view, he is specialized in the measurement and monitoring of deformations using differential interferometric SAR techniques. He has been involved in a number of projects of the 5th, 6th, 7th and H2020 Framework Programmes of EU and in different ESA-funded projects. His research interests include the analysis of spaceborne, airborne, and ground-based remote sensing data and the development of scientific and technical applications using active sensor types.

Dr. Crosetto was the recipient of the Best Young Author of the 20th ISPRS Congress Award, in Istanbul, in 2004. He is Cochairman of the WG III/3, "SAR-based surface generation and deformation monitoring" of the ISPRS.